공학박사학위논문

# 딥러닝 기반 와류기인 선박 프로펠러 진동 탐지 기술

**Deep learning-based detection technology for vortex-induced vibration of a ship’s propeller**

2022년 8월


서울대학교 대학원

기계항공공학부

임 도 형

# 딥러닝 기반 와류기인 선박 프로펠러 진동 탐지 기술

**Deep learning-based detection technology for vortex-induced vibration of a ship's propeller**

**지도교수 김 윤 영**

**이 논문을 공학박사 학위논문으로 제출함**

2022년 4월

**서울대학교 대학원**

**기계항공공학부**

**임 도 형**

**임도형의 공학박사 학위논문을 인준함**

2022년 6월

**위 원 장 :** 윤 병 동 (인)

**부위원장 :** 김 윤 영 (인)

**위 원 :** 김 도 년 (인)

**위 원 :** 장 강 원 (인)

**위 원 :** 선 경 호 (인)

# ABSTRACT

## Deep learning-based detection technology for vortex-induced vibration of a ship's propeller

Do Hyeong Lim
School of Mechanical and Aerospace Engineering
The Graduate School
Seoul National University

Due to the International Maritime Organization's (IMO) regulations on carbon emission reduction, the shipbuilding and shipping industry increases the size of ships and adopts energy-saving devices (ESD) on ships. Accordingly, design changes of underwater structures such as propellers, rudders, and ESD of ships are required in line with these trends. The lock-in phenomenon caused by vortex-induced vibration (VIV) is a potential cause of vibration fatigue and singing of the propellers of large merchant ships. The VIV occurs when the vibration frequency of a structure immersed in a fluid is locked in its resonance frequencies within a flow speed range. Here, a deep learning-based algorithm is proposed for early

detection of the VIV phenomenon. A salient feature in this approach is that the vibrations of a hull structure are used instead of the vibrations of its propeller, implying that indirect hull structure data relatively easy to acquire are utilized. The RPM-frequency representations of the measured vibration signals, which stack the vibration frequency spectrum respective to the propeller RPMs, are used in the algorithm. The resulting waterfall charts, which look like two-dimensional image data, are fed into the proposed convolutional neural network architecture. To generate a large data set needed for the network training, we propose to synthetically produce vibration data using the modal superposition method without computationally-expensive fluid-structure interaction analysis. This way, we generated 100,000 data sets for training, 1,000 sets for hyper-parameter tuning, and 1,000 data sets for the test. The trained network was found to have a success rate of 82% for the test set. We collected vibration data in our laboratory's small-scale ship propulsion system to test the proposed VIV detection algorithm in a more realistic environment. The system was so designed that the vortex shedding frequency and the underwater natural frequency match each other. The proposed VIV detection algorithm was applied to the vibration data collected from the small-scale system. The system was operated in the air and found to be sufficiently reliable. Finally, the proposed algorithm applied to the collected vibration data from the hull structure of a commercial full-scale crude oil carrier in her sea trial operation detected the

propeller singing phenomenon correctly.

**Keywords: Ship propeller vibration, Vortex-induced vibration(VIV), Vibration-based monitoring, Deep learning(DL), Convolution neural network(CNN)**

**Student Number: 2013-30770**

# CONTENTS

# LIST OF TABLES



# LIST OF FIGURES

# CHAPTER 1.
# INTRODUCTION

## 1.1. Motivation

Due to the increase in international trade, exhaust gas from ships is pointed out as the main cause of environmental pollution, and the demand for eco-friendly ships is also increasing rapidly in the shipbuilding and offshore field. The International Maritime Organization (IMO) aims to reduce the carbon emissions of ships by more than 30% compared to 2008 by 2025 and by more than 70% by 2050. Accordingly, various efforts are being made in all directions in the shipbuilding and shipping industry to respond to IMO regulations. Eco-friendly fuel, electric propulsion system, autonomous navigation technology including route optimization, installation of stern attachments to reduce fuel, and enlargement of ship size are some of these efforts. The first is the design change of underwater structures.

Also, as the size of the vessel progressed rapidly, as shown in the Fig. 1.1, 10 years ago, it was the largest vessel capable of carrying up to 10,000 20ft container boxes, but more than 22,000 very large container carriers have been built and operated in recent years. Fig. 1.2 shows the propeller of a super-large ship over 10m that did not exist before. Design changes due to the rapid increase in size are causing various design problems that were not previously present. Most structural

damage problems occur in underwater structures such as propellers, rudders, and ESD (Energy Saving Device) as shown in the Fig. 1.3. In the case of an underwater structure, since the specific gravity of water is 1,000 times greater than that of air, the size of the applied load is large, and for efficiency, it has a slender airfoil shape, so it is structurally weak. Recent advances in CAE technology are filtering out most of the vibration and fatigue strength issues at the design stage. However, in the case of fatigue problems of underwater structures, it is difficult to accurately predict fatigue damage because large-sized structures have to be solved due to fluid and structural coupling problems. In particular, as shown in Fig. 1.3, in the case of a ship with ESD installed, the flow field is much more complicated than that without ESD, making it difficult to analyze and has a high probability of structural damage.

Fig. 1.4 shows a typical underwater structure design procedure. Since the size of the structure has increased significantly compared to the previous one, and additional structures was added, a careful review is required at the design stage. The basic design of a structure usually uses a calculation sheet containing design know-how. In this calculation sheet, the necessary values to satisfy the performance and structural strength according to the design requirements should be entered. When the 3D shape is derived through the design program, the hydrodynamic performance is reviewed through computational fluid analysis. In the case of propellers, cavitation problems must also be filtered out at this stage. Since the performance of the propeller is most important, it should be verified

through a model test in a water tank. Static and dynamic loads calculated through computational fluid dynamics are used to calculate static and fatigue strength of underwater structures. In addition, it is designed to avoid resonance with main vibratory forces and structures through vibration analysis. When it is confirmed that the structure has a sufficient fatigue life, the construction of the structure begins. In the case of propellers, they are made of casting, and defects are detected and repaired through various non-destructive tests. The final stage is the ship commissioning stage. In the trial run stage, the performance of the structure, such as the speed of the ship, is verified, and the design feasibility is verified by comparing the predicted vibration value with the measured value.

The propeller of a ship works by turning the blades in the shape of airfoil and generating lift using the rotational energy generated by the main engine. The propeller of a large merchant ship, as shown in Fig. 1.5 [1], is made of copper casting and is designed to have a sufficient structural safety factor during the lifespan of the device, taking into account the static load and variable load applied to the structure [2]. Nevertheless, in some cases, propellers that are exposed to severe loads under diverse operating conditions are damaged before the projected lifespan comes to an end [3]. Fig. 1.5 shows examples of damage to other underwater structures such as ESD and rudder as well as propellers.

Fig. 1.6 shows the procedure for identifying the cause of damage to underwater structures. In order to understand the root cause of damage to underwater structures, the first step is to inspect the damaged surface. Damage

surface examination plays an important role in the analysis of the cause of damage. The second process is to verify the load acting on the actual structure. It is very important to accurately understand the load on the structure, and damage occurs when a load greater than the assumed design load acts on the structure for various reasons. Methods of measuring the load of a structure will be dealt with in the next chapter. When a load with different characteristics from the design load is measured, the structural strength and fatigue life are recalculated using the measured load. Through this calculation, it is possible to estimate whether the damage to the underwater structure is a design problem or a manufacturing defect.

Usually, the cause of damage to a propeller that has not reached the end of its design life is a manufacturing defect, an incorrectly selected material, or an incorrectly assumed design load. In particular, in the case of damage to underwater structures, most of the cases are caused by incorrectly assumed design loads, because it is difficult to sufficiently consider the load characteristics of underwater structures at the design stage. In general, the static load can be predicted relatively accurately because it is proportional to the power of the propeller. However, in the case of dynamic load, the change in size is very large due to changes in the complex surrounding flow field or structural differences due to production tolerances.

One of the main causes of underwater structural failure is vortex-induced vibration (VIV) [3]. Fig. 1.7 shows the vortex shedding phenomenon in a 2D cylinder [4]. The cycle of vortex shedding is constant at a specific flow velocity,

and it excites the structure on a constant cycle. Fig. 1.8 shows the formula for calculating the vortex shedding frequency. The vortex shedding frequency is proportional to the Strouhal number, a dimensionless number related to the shape of the structure, proportional to the inflow velocity of the flow, and inversely proportional to the effective thickness of the trailing edge. When the foil shape and flow velocity are determined, the vortex shedding frequency is calculated. Empirically, the range of the actual frequency is 90%~110% of the predicted value due to the uncertainty of each variable.

If the vortex shedding frequency coincides with the natural frequency of the structure, the excitation force caused by vortex shedding excites the vibration mode of the structure, greatly increasing the vibration response. The vibration of the structure, thus increased, makes the vortex shedding phenomenon stronger, which also increases the vibration response. When VIV occurs in an underwater structure, the resonance frequency at which the initial VIV is generated is maintained even though the operating conditions change slightly due to the strong interaction between the flow and the structure; this effect is referred to as the “lock-in phenomenon” [5,6]. Fig. 1.9 explains the concept of lock-in phenomenon that occurs when the vortex shedding excitation frequency coincides with the natural frequency of the structure. Large amplitude oscillations occur when the vortex shedding and the structural vibration frequencies coincide, a condition referred to as ‘lock-in’. The lock-in condition can occur over a range of oncoming flow velocities and the vortex shedding frequency can be driven relatively far from the

Strouhal frequency, which results from the von Kármán instability behind a stationary cylinder; this phenomenon of frequency entrainment is described as ‘wake capture’. The lock-in phenomenon is a kind of self-excited vibration in which the coupling between flow and propeller structure vibration is strongly generated. As shown in Fig. 1.10, the resonance caused by lock-in has a wider range than general resonance, and it has hysteresis characteristics with different vibration patterns when the operation speed increases and when the operation speed decreases.

High-frequency VIV in the propeller of a large merchant ship causes a propeller singing phenomenon, which is a common abnormal noise problem associated with ships, whereas low-frequency VIV causes an engine room vibration problem and leads to damage caused by vibration fatigue rather than a noise problem as the vibration displacement is large [3,7,8]. That is to say, when the vibration fatigue exceeds the fatigue limit of the material due to the lock-in caused by propeller VIV, vulnerable parts of the ship get damaged. Accordingly, though it is important to design propellers to prevent lock-in, it is very difficult to predict whether VIV and lock-in will occur or not during the design phase as the flow coming into a propeller is not uniform due to the complicated shape of the stern as shown in Fig. 1.11[3].

In addition, since the vibration response in a structure where resonance occurs rapidly increases at the resonance point, even propellers manufactured with the same design have large variations in vibration response depending on

manufacturing tolerances, etc. This is the reason why the damaged propeller and the non-prone propeller coexist in 10 propellers manufactured with the same design.

Accordingly, resonance avoidance design is done during the design phase in a shipyard using a vortex shedding frequency that is predicted with an empirical formula, and whether the lock-in phenomenon will occur is assessed by measurements taken during the ship's sea trial. If lock-in caused by propeller VIV is found in the sea trial phase, the vortex shedding frequency is changed (because it is difficult to change other design conditions of the propeller), usually by changing the air foil trailing edge of the propeller, to solve the resonance problem as shown in Fig. 1.12[7]. Fig. 1.13 shows an example of lock-in caused by propeller VIV; the vibration problem was fixed by correcting the trailing edge of the propeller. Measuring the vibration when lock-in has occurred shows that a high response is maintained at a specific frequency even when the rotational speed of the propeller changes. If the lock-in phenomenon is not screened for during the sea trial process, the ship will be delivered to its owner as is, leading to enormous financial loss to the shipyard as a result of reproduction and redocking of the propeller because the propeller will fail before it reaches the intended lifespan. Accordingly, it is very important to check whether or not lock-in caused by propeller VIV occurs during the sea trial phase of a ship [7].

## 1.2 Research Objectives

The purpose of this paper is to find a method to easily and accurately measure structural vibration, which is a vortex, which is a representative cause of damage to underwater structures. To this end, we would like to propose a technique for diagnosing vortex induced vibration based on deep learning, which shows excellent performance in the recent image detection field. Because it is difficult to obtain measurement data for underwater structures where vortex induced vibration occurs and it is difficult to obtain sophisticated prediction data by solving the fluid-structure coupling problem, a simple model based on vibration theory is used to obtain 10,000 data sets required for learning. was able to obtain In addition, we want to show that it is possible to generate a vortex-like vibration through a reduced model test and detect it through the algorithm proposed in the paper. In addition, we intend to verify the applicability of the proposed algorithm using the structural vibration values measured in actual large commercial ships.

## 1.3 Outline of thesis

Since it is difficult to confirm the VIV problem at the design stage, it is absolutely necessary to check it through measurement in the test run stage just before delivery of the ship. In Chapter 2, we reviewed the vibration measurement method of structures, and in particular, the method of measuring vibration of underwater structures, which is very difficult to measure because radio waves are not transmitted, was considered. The traditional method of measuring the load acting on a structure is to directly measure the strain of the structure by installing a strain gauge on the structure and installing an underwater telemetry, but the problem is that it takes a lot of money for measurement and the probability of measurement failure is very high. there is In this paper, we proposed a method to indirectly detect vortex induced vibration, which is a major cause of damage to propellers of large merchant ships, through hull vibration measurement in the test operation stage. If the specific VIV is a problem, when the vortex shedding frequency at the flow rate matches the natural frequency of the structure, the vortex shedding strength increases due to resonance and the lock-in phenomenon occurs in which the vortex shedding frequency is maintained even if the flow speed increases. This is because indirect measurement can explicitly confirm this. To this end, iterative vibration measurement and evaluation process by a vibration expert is required. Chapter 3 describes the development of deep learning algorithms for VIV diagnosis. In this study, a CNN (Convolution Neural Network) algorithm, which is

widely used for image-based object detection, was used to automate diagnostic VIV detection. In this study, object detection is performed but classification is not required, so to develop a specialized CNN model, 30 CNN models were reviewed by adjusting the hyperparameter to increase the hidden layer. Finally, detection performance without overfitting We proposed a model with this high five hidden layers. In order to generate large-scale data required for CNN learning, a simple ship model based on the vibration mode superposition method was proposed and propeller vibratory force was simulated. Using a simple model, 10,000 pieces of data showing vibration characteristics similar to the actual vibration measurement results were generated and used for learning. As a result of testing using 1,000 pieces of data, it was able to show a diagnosis success rate of over 82%. In Chapter 4, a reduced model test was performed to verify the proposed diagnostic system. Using a reduced model of the ship propulsion system including a 1/10 scale propeller designed to match the vortex shedding frequency and the underwater natural frequency of the blade, vortex induced vibration is generated from the propeller, and the Vibration was measured. It was confirmed that the detection system developed in this study can detect VIV generated in the reduced model. In Chapter 5, the feasibility of the developed diagnostic system was verified using the vibration values of the hull structure measured in the engine room during the trial operation of a 3,000-ton crude oil carrier that had a propeller VIV problem, and its applicability to actual ships was also confirmed. In Chapter 6, the conclusion remarks for this research will be presented.

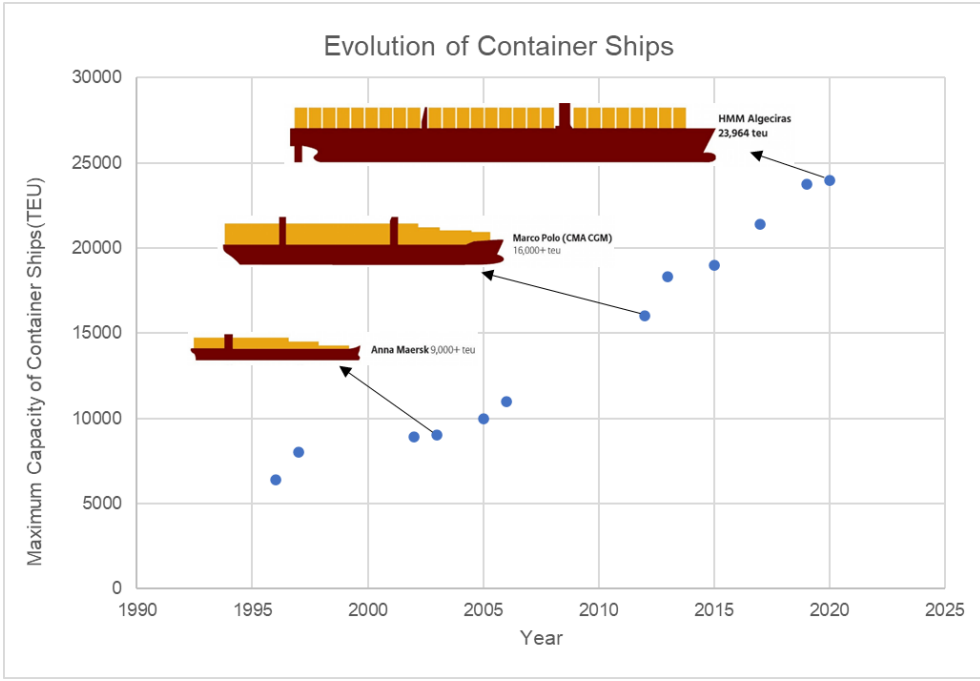


**Fig. 1.1** Increase of maximum capacity of container carrier

**Fig. 1.2** Ship propeller [1]

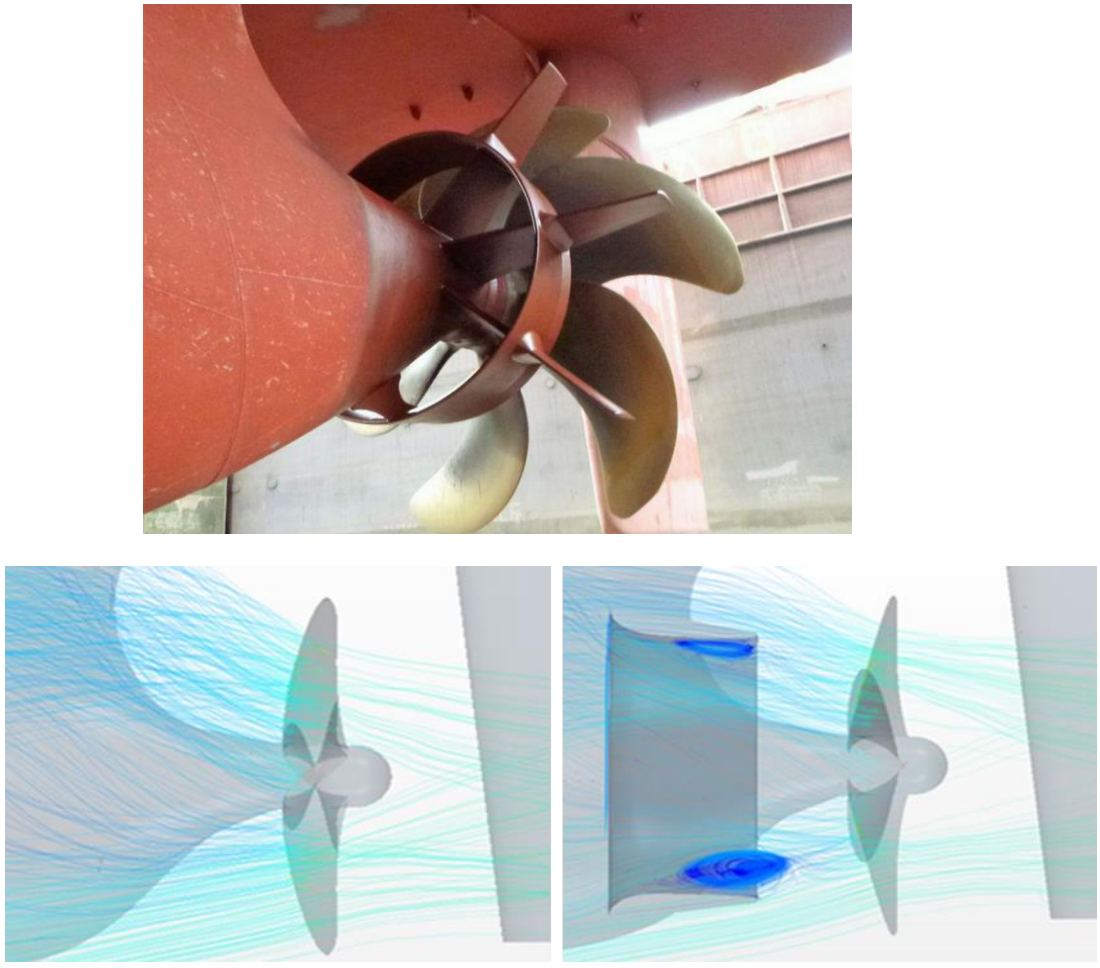

**Fig. 1.3** Change of the flow field around the stern structure by installing energy saving device

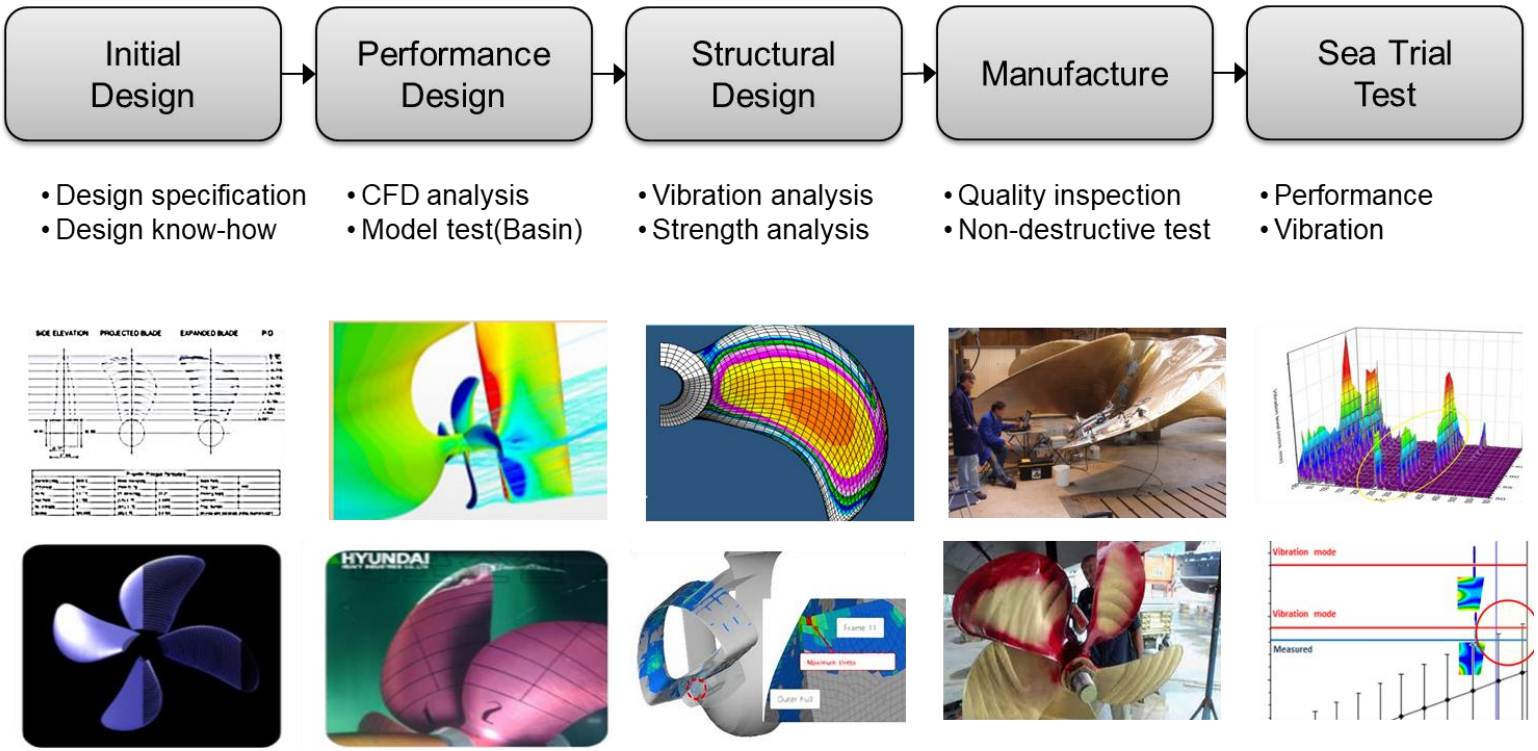


**Fig. 1.4** Underwater structure design process

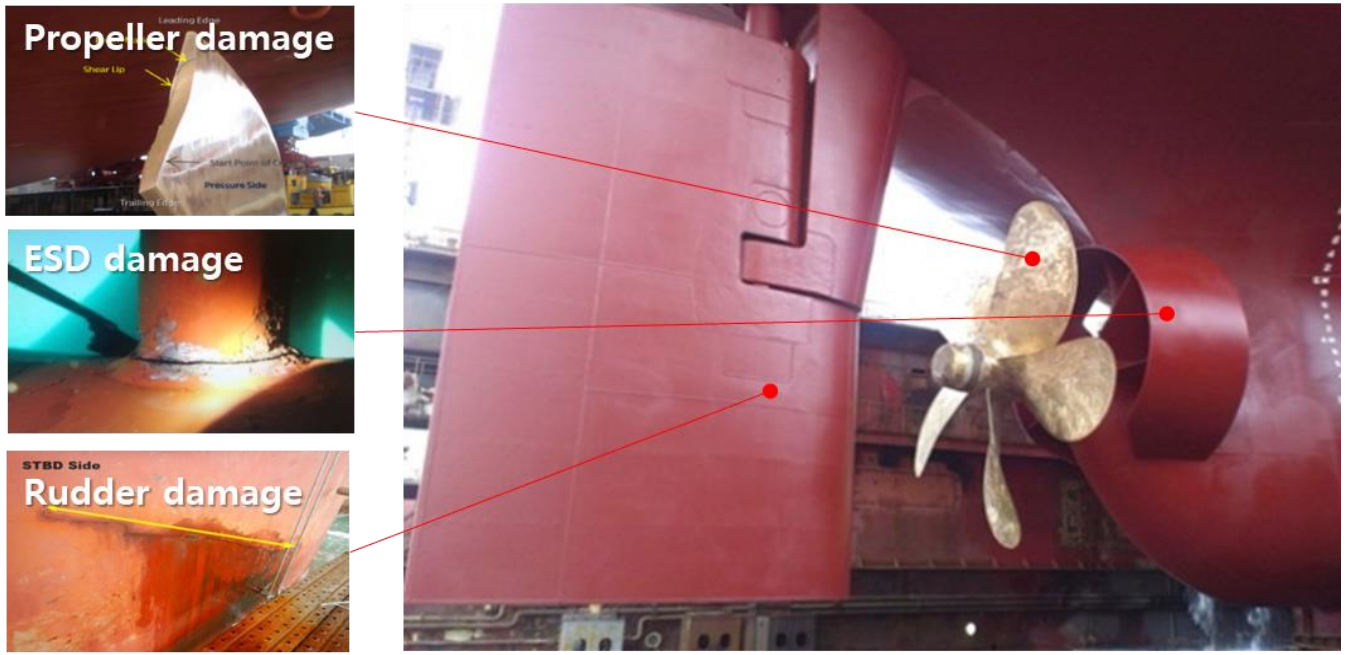


**Fig. 1.5** Damage of underwater structure

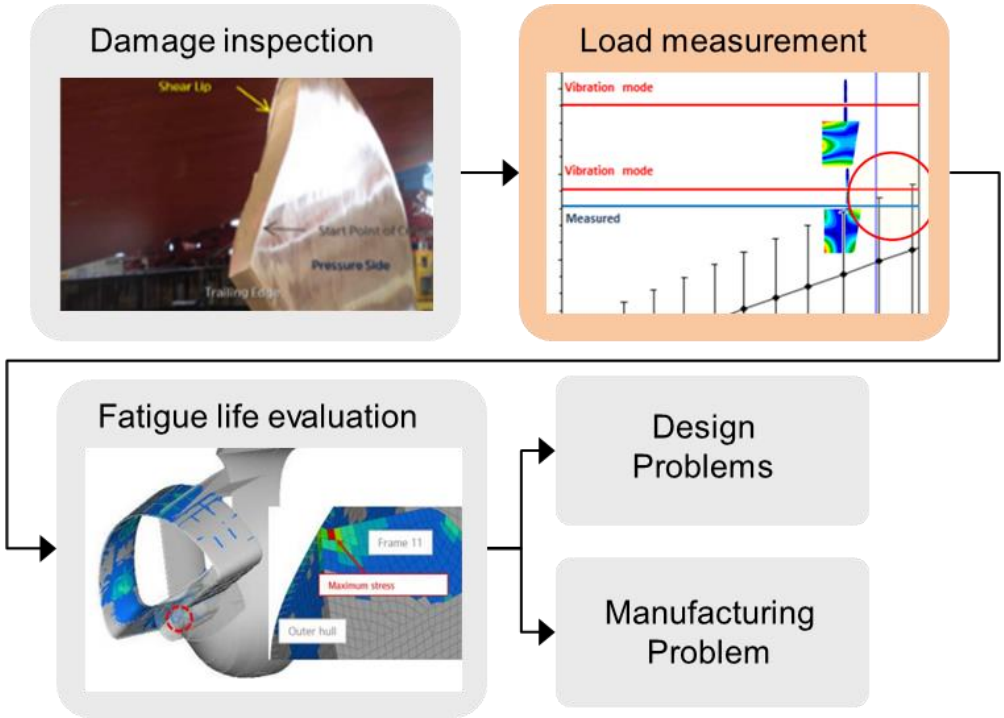


**Fig. 1.6** Root cause analysis for structural failure

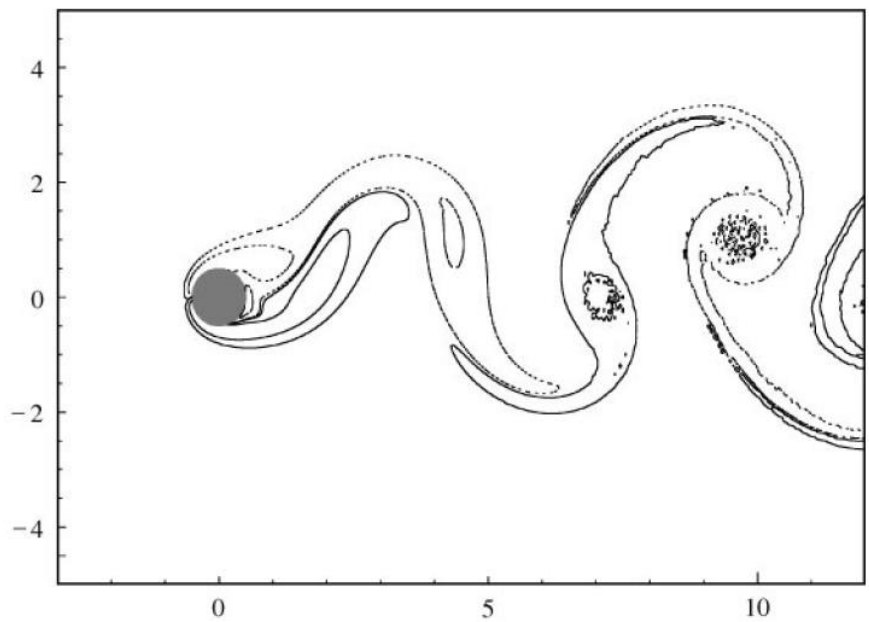


**Fig. 1.7** Vorticity of 2D cylinder (coordinates normalized by cylinder diameter)

[4]

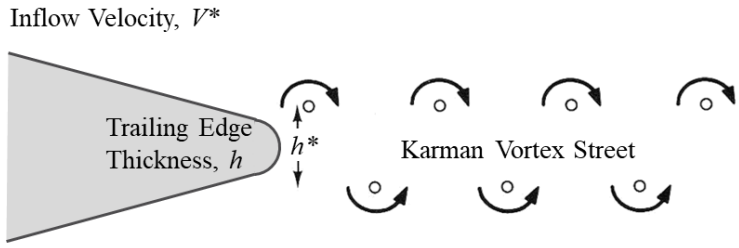


$$f_s = \mathrm{St}\frac{V^*}{h^*}$$

where $f_s$ : Vortex Shedding Frequency [4)]
$\mathrm{St}$ : Strouhal No. [1)]
$V^*$ : Inflow Velocity [2)]
$h^*$ : Effective TE Thickness [3)]

1) Strouhal number depends on the geometry of TE (TE angle, bluntness, etc.), Reynolds number and other details in the flow.
2) Inflow velocity is predicted by using ship speed and nominal wake distribution.
3) Effective TE thickness is calculated by summation of geometrical TE thickness and pressure/suction boundary layer thickness.
4) It is assumed that actual vortex shedding frequency resides within the range of 90%~110% of the predicted due to uncertainty in St, V*, h* values.

**Fig. 1.8** Calculation of vortex shedding frequency

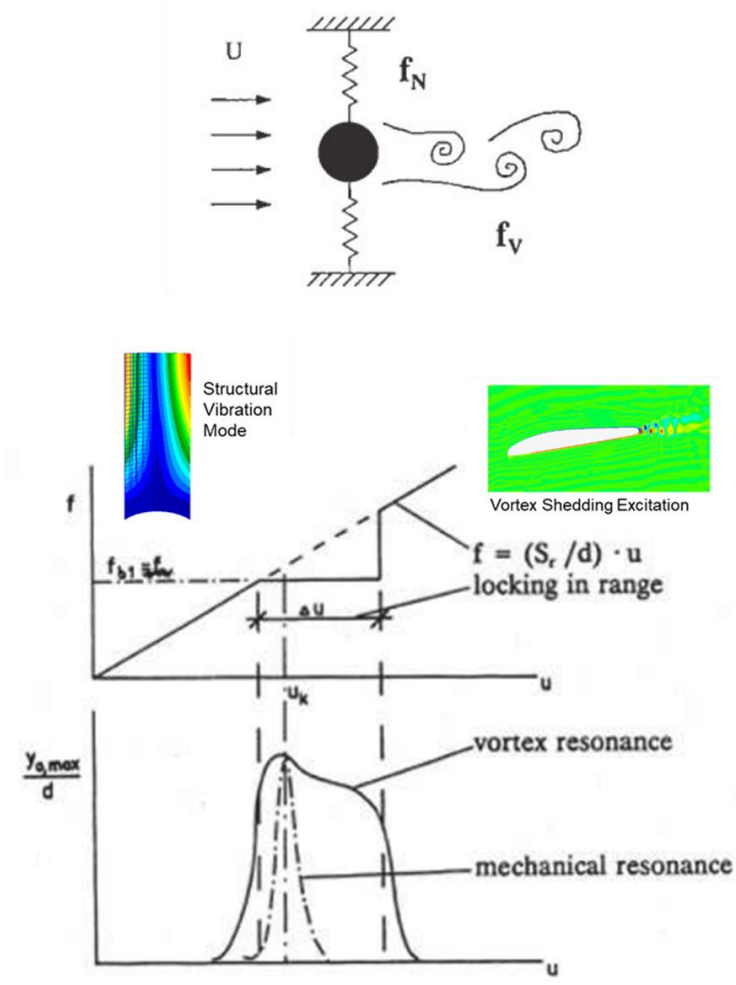


**Fig. 1.9** Concept of vortex shedding excitation and lock-in phenomena

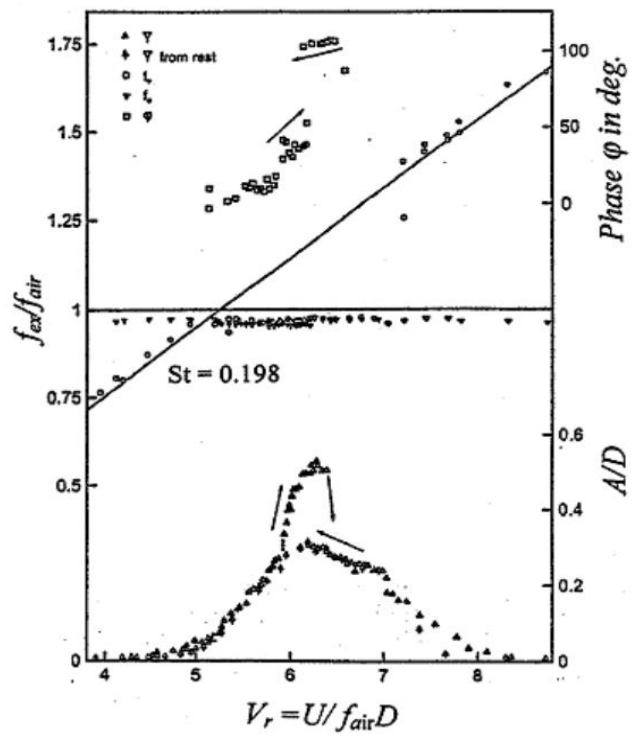


**Fig. 1.10** Vortex shedding lock-in oscillation[4]

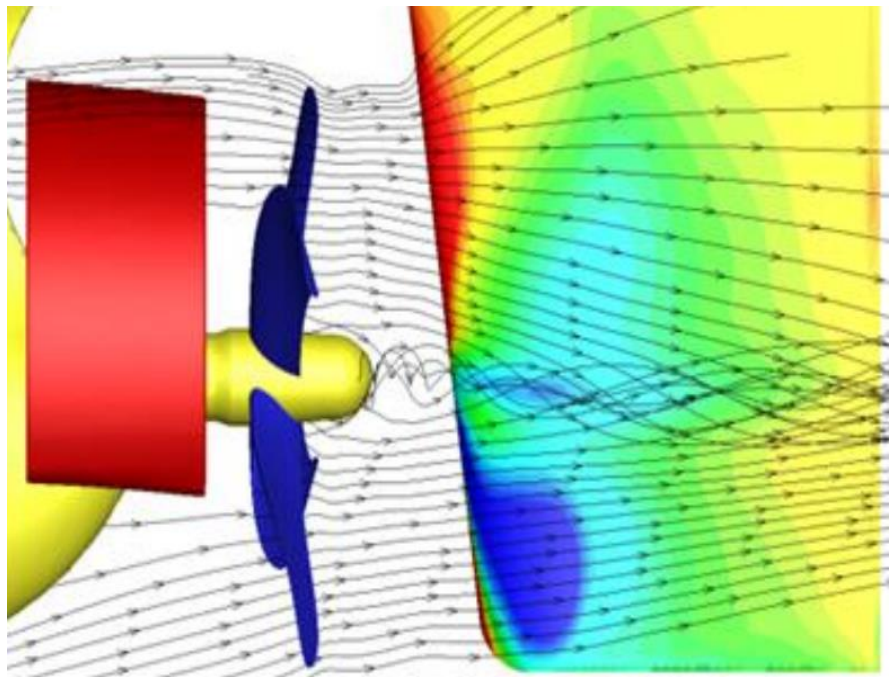

**Fig. 1.11** Complexity of the flow field around stern structures

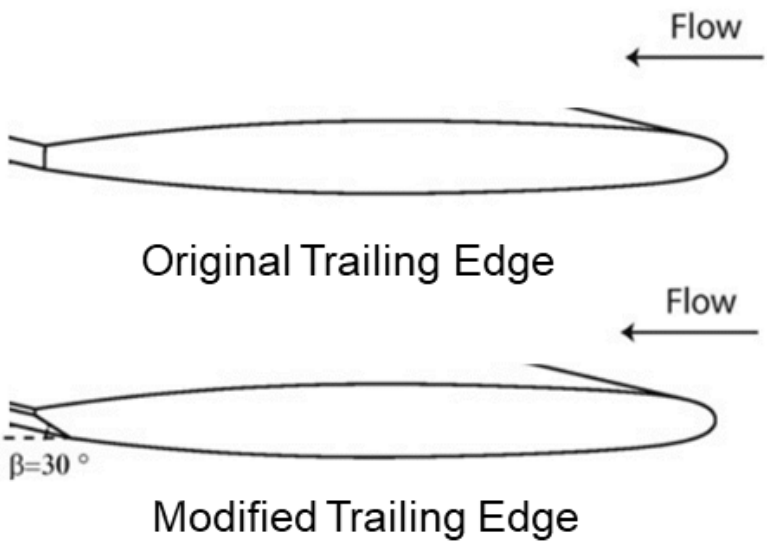


**Fig. 1.12** Example of propeller trailing edge modification

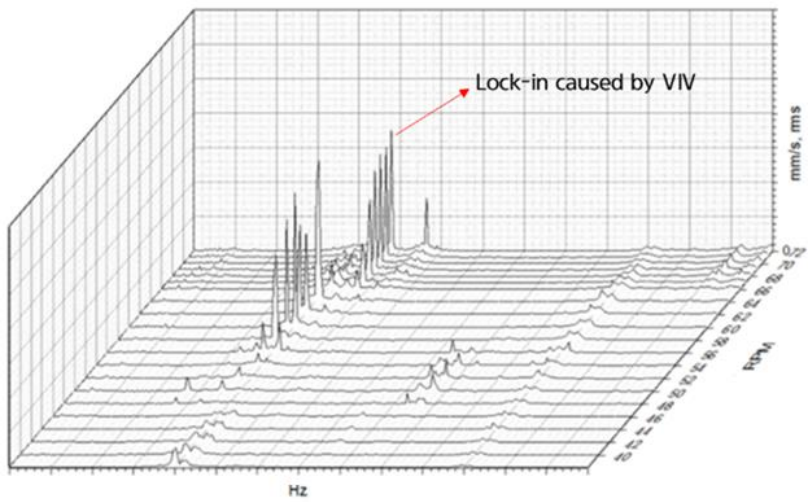


(a)

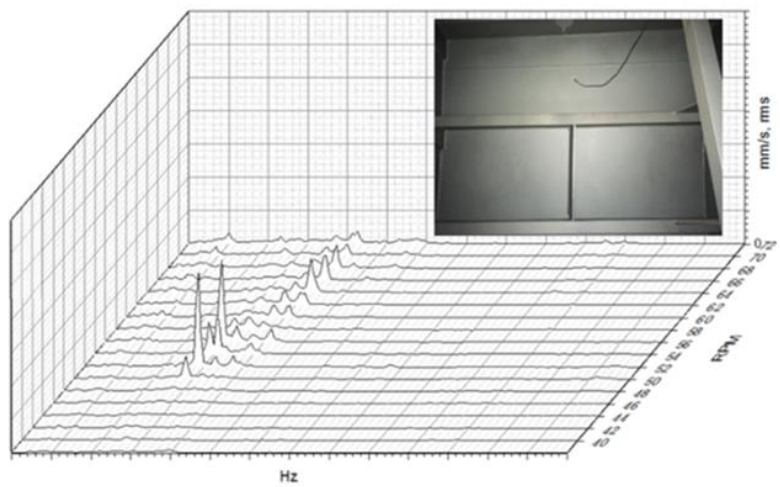


**(b)**

**Fig. 1.13** Vibration measurements before and after propeller modification (a) Lock-in caused by ship propeller VIV; (b) After propeller trailing edge modification

# CHAPTER 2.
# PROPELLER VORTEX-INDUCED VIBRATION MEASUREMENT METHOD

## 2.1. Structural vibration measurement methods

A method of measuring the vibration of a structure includes a method of measuring a displacement of a structure or a method of measuring velocity and acceleration. In general, the measurement method is determined according to the ease of sensor installation, the frequency of interest, and the magnitude of the vibration. The most general type of vibration sensor is an accelerometer, and there are two types: a cantilever type with a strain gage installed inside and a piezo-electric type using piezoelectric phenomenon. When the frequency is relatively low, an electro-magnetic velocity meter that directly measures the speed is sometimes used, but it is a method that is not used much these days. A general method to measure the velocity is a method using a laser doppler velocimeter (LDV), which measures the surface velocity of a structure using the Doppler effect. The last method is to measure displacement. Eddy current type or capacitive type non-contact displacement sensors are often used to measure the displacement of structures. Recently, because of the ease of installation, the displacement is often

measured using a laser. Also, recently, there is a case in which a high-speed camera is used to measure the vibration of a low-frequency structure with a large displacement. IMU (Inertia Measuring Unit) is often used for small structures. It is mainly used for control purposes, but it is also used for monitoring purposes. The most representative purpose of measuring the vibration of a structure is to predict the lifespan of the structure, and therefore the most direct vibration measurement method is to directly measure the dynamic strain using a strain gage. The measured dynamic strain is used to calculate the fatigue safety factor of the structure.

## 2.2. Direct measurement method for propeller vibration

Underwater structures such as propellers, rudders, and ESD are important structures for ships, and vibration measurement is necessary for design verification or life prediction. For vibration measurement of underwater structures, shipyards are considering various measurement methods and using them. The traditional method of measuring the lock-in phenomenon generated by a propeller and the resulting stress acting on the structure is shown in Fig. 2.1 [2]. After strain gauges are installed on a rotating propeller and the cables of the strain gauges are connected to the ship's interior through a hollow shaft, information is delivered to a stationary data storage device through telemetry or a slip ring. Though underwater telemetry has the advantage of not necessitating the hollow shaft, it has a limitation: cables for signal transmission must penetrate the shell of a ship. As a highly variable amount of pressure is applied to the surface of a propeller, to make strain gauges stick tightly to the propeller without creating a waterlogging problem, specialized equipment such as a welding gauge or techniques such as silicone application are required. Despite such efforts, as it is difficult to measure the stress of a rotating underwater structure and attempts to do so often fail, this cannot truly be regarded as an efficient and promising method of checking propeller lock-in in the sea trial phase of a ship because it must be repeated several tens of times per year. Another method to directly measure the vibration of the propeller is to make a

transparent observation window on the bottom of the hull where the structure is visible and measure the vibration of the structure using a laser velocimeter as shown in Fig. 2.2. In order to observe the cavitation of the propeller, some shipowners make a transparent observation window at the bottom of the ship. The idea is to measure the vibration of the propeller with a laser velocimeter through this observation window. In order to measure the vibration of a rotating propeller, a signal processing technique that uses a tracing device or performs sampling according to the number of rotations is also required, and there is a problem in that it is affected by turbidity of seawater or floating matter. Also, above all else, the biggest problem is the need to make an observation window due to the problem of water leakage and structural strength.

## 2.3. Indirect measurement method for propeller vibration

The calculation of the vortex shedding frequency is much more elaborate and requires 3D flow field analysis [9] and, if the vibration displacement is large, it is difficult to analytically predict the vortex shedding frequency as fluid-structure interaction analysis is required [10]. Accordingly, we need a simple and highly reliable measurement method that can replace the strain gauge-based direct measurement method of assessing the occurrence of VIV in the sea trial phase of the ship such that the appropriate actions can be taken before delivery of the ship.

Fig. 2.3 explains the mechanism by which the flow field is excited by the vortex induced vibration and the vibration is transmitted to the accelerometer as the flow field excites the hull structure. Because the propeller flow field is large enough to generate the thrust of the ship, the propeller fluctuating pressure becomes one of the main vibratory forces exciting the hull. Therefore, when an abnormal vibration component occurs in the propeller, the vibration component excites the surrounding flow field, and the generated fluctuating pressure is transmitted to the inside of the hull in the form of structural vibration. In the shipyard, it was confirmed empirically that, when vortex induced vibration occurred, the vibration component generated by VIV in the ship's internal structure could be clearly measured. In addition to the vibration component transmitted through fluid excitation, as shown in Fig. 2.3, there may be vibration components

transmitted through the propeller, shaft system, bearing, and hull path. As a result of the test using the reduced model in Chapter 4, it was found that the magnitude of the propeller vibration component transmitted through the shaft system with very high impedance is very small, and the component transmitted through fluid excitation is the main component of the internal acceleration of the vessel.

Fig. 2.4 shows a sample vibration spectrum measured at the hull by an accelerometer inside a ship. Vibration of the propeller component, which is the dominant component of the ship's stern, is readily observed; the vibration is generated as a result of vibration of the propeller, which is delivered to the hull when the hull structure is excited through the fluid, and by exciting the structure through the shaft and bearing. This result suggests that occurrence of propeller VIV can be assessed by measuring the vibration of the hull points near the propeller.

When VIV grows and structure-fluid coupling vibration occurs, lock-in occurs, and most fatigue damage problems are related to this. Therefore, the occurrence of lock-in itself is a problem, and it is possible to determine whether lock-in has occurred using the waterfall chart. Fig. 2.5 shows a typical waterfall diagram when lock-in occurs. As the natural frequency of the propeller coincides with the vortex shedding frequency, the magnitude of the vibration increases rapidly, and the resonance frequency is maintained despite the change in the rotation speed of the propeller. can be clearly identified. For lock-in diagnosis, an

expert's evaluation is required, and the expert examines the measured waterfall chart one by one to determine whether resonance and lock-in occurs. This consumes time and money, and there are cases where the lock-in phenomenon cannot be detected due to human error due to repetitive tasks. In the case of large shipyards, since more than 100 ships are built a year and it is difficult to determine whether lock-in has occurred by collecting and analyzing long-term data each time, a diagnostic system that can automatically determine whether or not lock-in occurs from data acquisition is required. To this end, we will introduce artificial intelligence technology. In this study, it is necessary to find out not only whether lock-in has occurred, but also the frequency and propeller rotation speed at which lock-in has occurred. So general machine learning classification methods used for machinery diagnosis, such as Support Vector Machine (SVM), Logistic Regression, and K-Nearest Neighbors (KNN), are not appropriate.

In this study, occurrence of VIV is determined through waterfall charts. It takes a great deal of time and money to grasp whether resonance or lock-in occurs by reviewing waterfall charts one by one and, in some cases, a lock-in phenomenon may be missed due to human error. Accordingly, there is a need for a diagnostic system that allows easy installation of sensors and automatic measurement of the occurrence of VIV. To this end, in this study, we aimed to develop a deep learning-based VIV diagnostic system using a waterfall chart instead of human expert as

shown in Fig. 2.6. In other words, the role of deep learning network in this study is not to replace the signal processing method, but to replace the role of experts in determining whether a Lock-in phenomenon occurs using the signal processing results. As deep learning CNN technology shows excellent performance for image recognition [11], we thought that deep learning CNN technology may also be effective for VIV detection because waterfall chart is 2-dimensional data like an image. To detect lock-in on a waterfall chart, the frequency and RPM that cause a vibration problem must be recognized. We developed a lock-in detector by regarding this as an object detection problem.

Though deep learning has been used to solve multi-physics problems for prediction of vortex-induced vibration resulting from interactions between fluids and structures [12], it seems to be of limited use in solving an actual 3D propeller lock-in problem. In some cases, computer vision and deep learning have been utilized with a large amount of data to diagnose the integrity of a mechanical structure. Some cases make use of time data measured by sensors [13,14], while other cases use an image of the structure [15]. Recently, deep learning algorithms have been used along with existing artificial intelligence algorithms to troubleshoot machines that contain mechanical elements, such as gears, bearings, etc. The faults of mechanical systems have been diagnosed by utilizing timing signals from the vibration of the system [16-18], and the causes of mechanical system failures have

been diagnosed using the input values of diverse physical quantities, including vibration [19,20]. Many methods of illustrating time and frequency vibration data – as a 2D image through STFT (short time Fourier transform), waterfall chart, or wavelet transform, for example – and applying deep learning algorithms to diagnose a mechanical system have recently been proposed [21-26]. Deep learning-based troubleshooting and fault diagnostic methods that rely on 2D images are used in diverse fields; similar methods should be applicable to VIV detection.

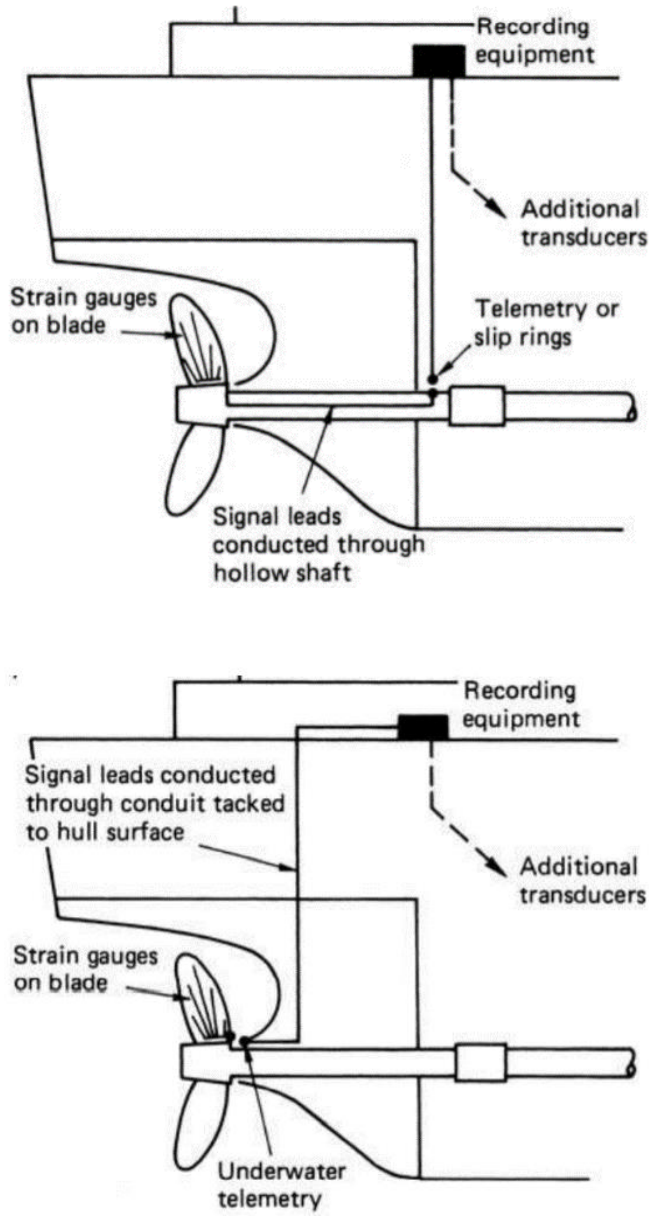


**Fig. 2.1** Strain measurement method for a ship propeller [2]

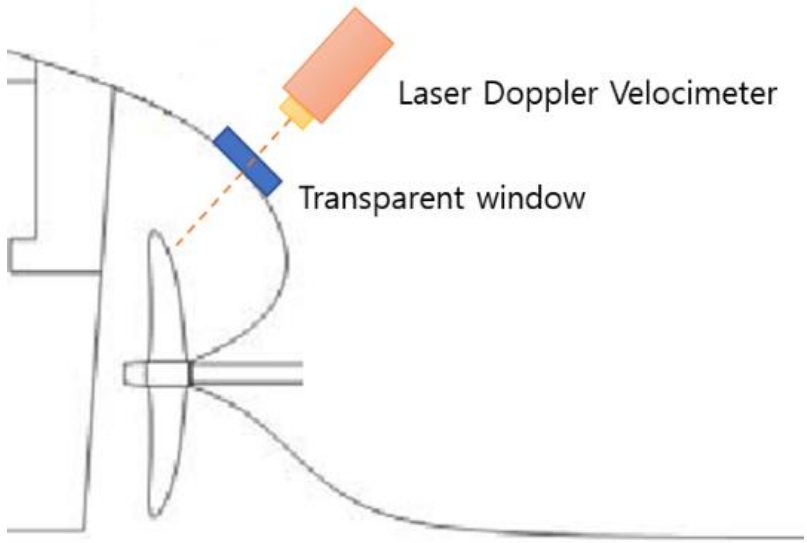


**Fig. 2.2** Laser doppler velocimeter measurement method for a ship propeller

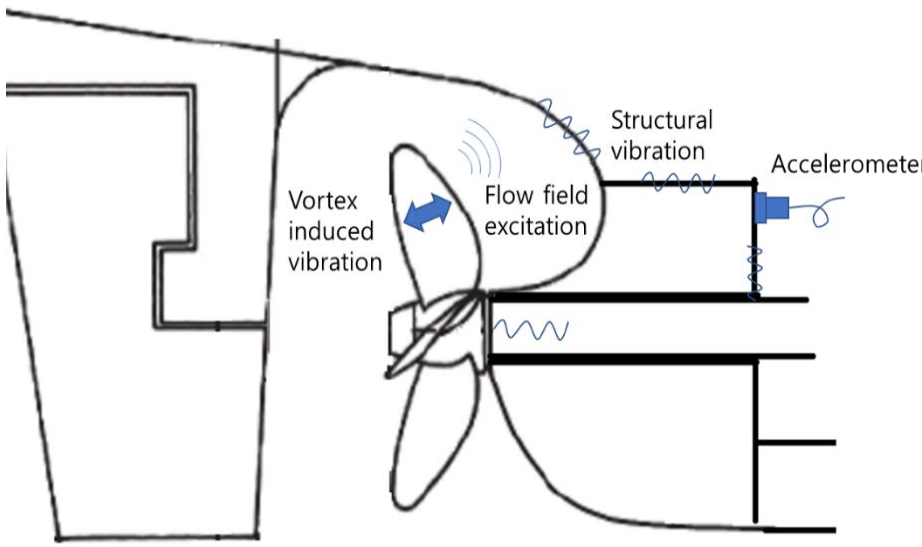


**Fig. 2.3** Transmission path of propeller induced vibration

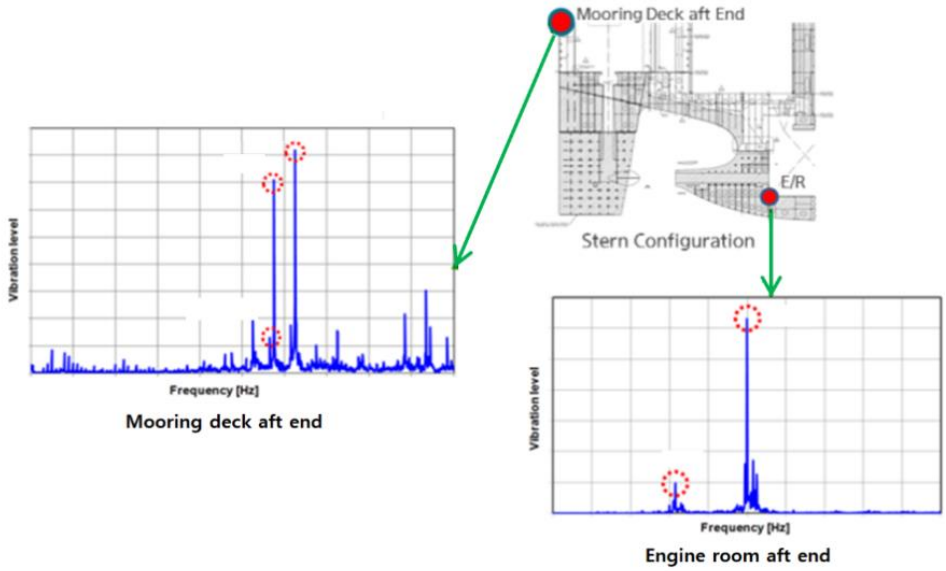


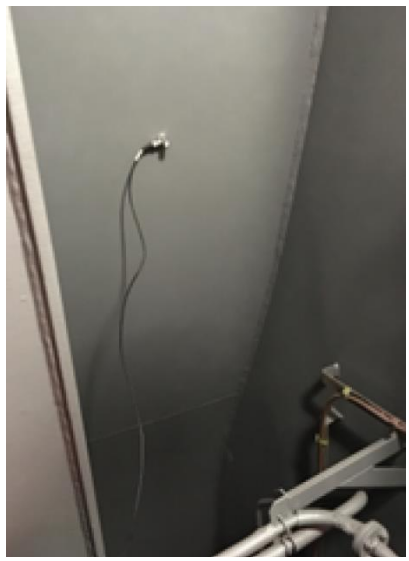

**Fig. 2.4** Harmonic component of propeller vibration measured at the stern

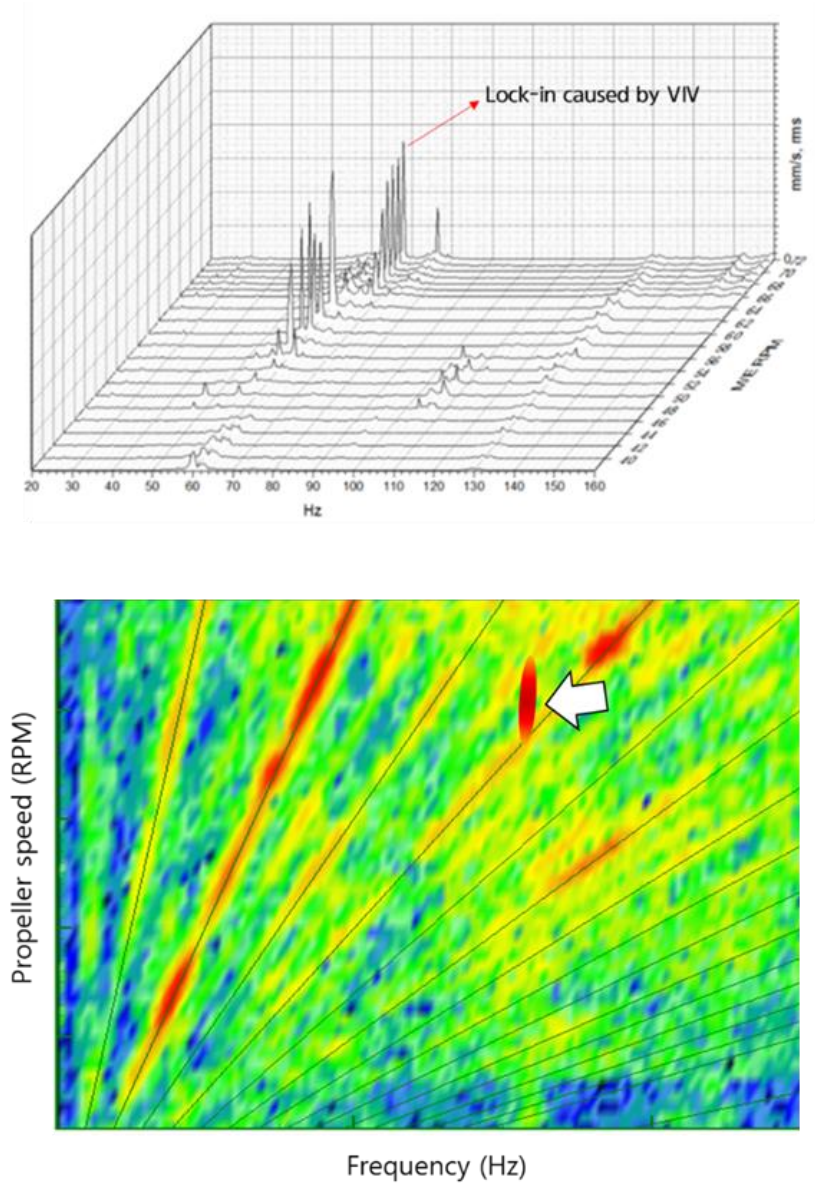


**Fig. 2.5** Example of measured vibration spectrogram when lock-in occurs

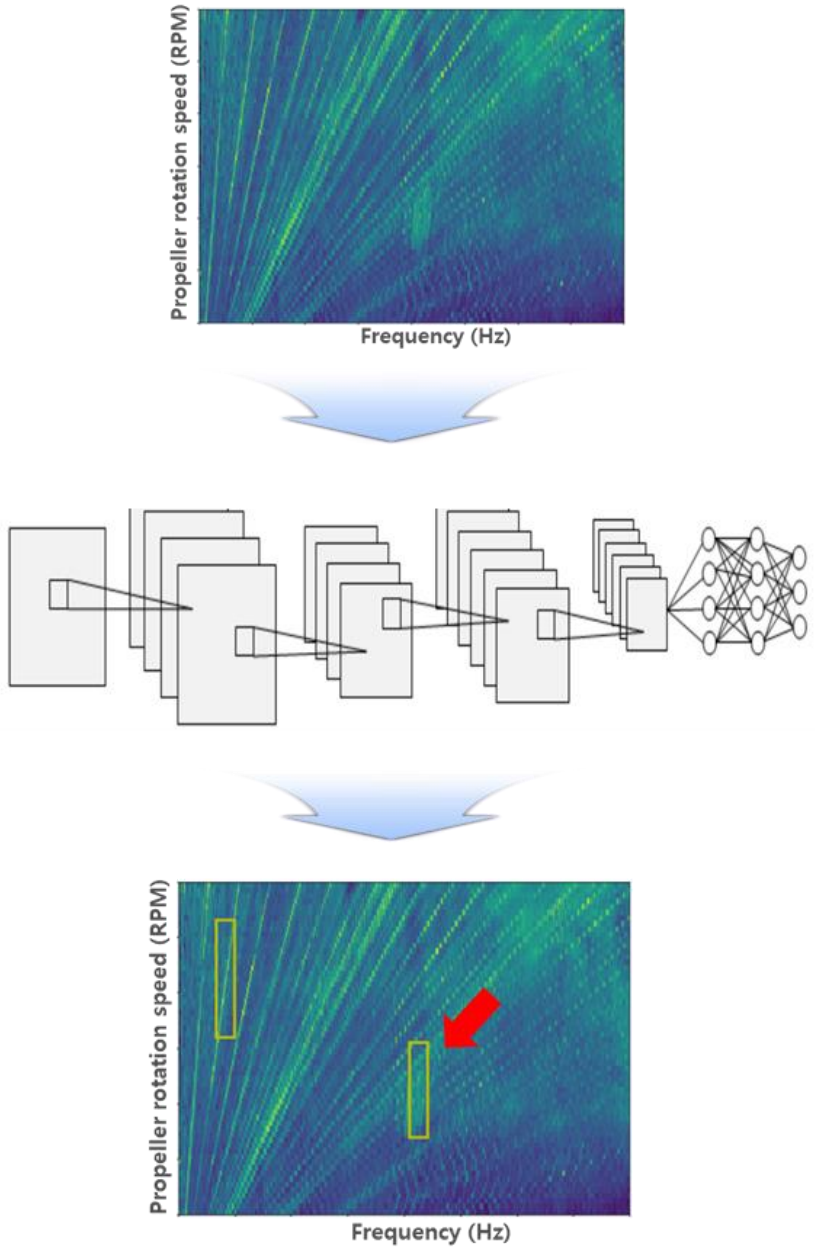


**Fig. 2.6** Schematic of CNN based VIV detection system

# CHAPTER 3.
# DEEP LEARNING NETWORK FOR VIV IDENTIFICATION

## 3.1. Convolution Neural Network

Among the many deep learning technologies, the Convolutional Neural Network (CNN) has been widely used in the various engineering fields due to its advantages such as parameter sharing, local connectivity, and the ability to consider high-dimensional information within the input data. CNN consists of a combination of several layers, including convolutional layers and pooling layers. Unlike traditional fully connected neural networks, CNNs use weight matrices of smaller dimensions than the input data, called kernels or filters. Therefore, CNNs have local connectivity properties that allow them to learn local patterns within small regions of the input data. Additionally, CNNs use multidimensional kernels to extract features, allowing them to consider high-dimensional information within the input data. In a convolutional layer, an output layer, called a feature map, with a depth equal to the number of kernels, is produced by sliding a kernel within the input data and performing a convolution operation. Based on these convolution operations, features are extracted from the input data. CNNs also use kernels with

equal weight values for these convolution operations within the entire input data. This is called parameter sharing. As a result, CNNs can significantly reduce the number of parameters to be trained and increase computational efficiency. Several types of convolutional layers are available depending on the dimensions of the input data. In general, a one-dimensional CNN using a one-dimensional kernel and a two-dimensional CNN (2D-CNN) using a two-dimensional kernel are used. A pooling layer pools a specific value (maximum or average) in a subregion. So the functional map of the previous layer is collapsed. Also, like other traditional neural networks, nonlinear functions are trained using nonlinear activation functions such as Rectified Linear Units (ReLUs). Finally, a fully connected layer that acts as a classifier follows. By stacking multiple combinations of these components, different CNN architectures can be achieved. Due to the advantages described above, the CNN method is widely used in various research fields such as face recognition, disease diagnosis, and natural language processing. Typical CNN structures are shown in Fig. 3.1.

**Convolution Layer**

The Convolutional layer consists of a set of filters. The values of these filters are the learnable parameters of the layer. The idea of a convolution when talking about CNNs is to extract the features from an image preserving the spatial

connection from the pixels and the learned features inside the image with the use of small equally-sized tiles. For an input image with size M×N×3 and the first convolutional layer K filters of size I×J where I <<< N and 3 represents the color channels. The learned features are a consequence of a mathematical operation between each element from the input image and the filter matrix. This is defined as:

$$u_{ij}{}^{l} = \sum_{a=1}^{A}\sum_{b=1}^{B} w_{ab}{}^{l}\, x_{i+a-1\ j+b-1}^{l-1} + b_{ij}{}^{l} \tag{3.1}$$

Where $u_{ij}{}^{l}$ is the value of feature map after convolution operation and before activation function, A is the height of a convolution filter, B is the width of a convolution filter, $w_{ab}{}^{l}$ is the weight parameter of convolution filters in the lth layer, $x_{ij}{}^{l-1}$ is the value of input image data in the lth layer, and $b_{ij}{}^{l-1}$ is a bias in the lth layer. In other words, the filter (also known as feature detector), slides through all elements of the image and is multiplied by each one producing the sum of multiplication that produces a single matrix named Feature Map. The depth together with the stride will control the size of the Feature Map matrix. Fig. 3.2 shows a convolution of a 5×5 image with a 3×3 filter matrix and stride of 1.

Additionally, an operation called ReLU (Rectified Linear Unit) is usually used as an activation function that adds non-linearity into the CNNs allowing it to

learn nonlinear models. It is an operation on top of each pixel that replaces all negative pixels inside the feature map by zeros. This rectifier technique is mostly used when compared with Hyperbolic Tangent or Sigmoid Functions since ReLU improves significantly the performance of CNNs for object recognition. ReLU function is described as follows.

$$x = \max(u, 0) \tag{3.2}$$

The output of the ReLU function is higher than one when the input value is higher than one.

**Pooling Layer**

As mentioned previously, pooling is one of the CNN distinctive concepts. The idea of the pooling step is to reduce the dimensionality of each feature map, eliminating noisy and redundant convolutions, and computation network yet retaining most of the important information.

$$u_{ij} = \frac{1}{A^2} \sum_{a=1}^{A} \sum_{b=1}^{A} x_{i+a-1\ j+b-1} \tag{3.3}$$

Where ${u_{ij}}^{l}$ is the value of feature map after convolution operation, A is the

height and width of a pooling area, $x_{ij}$ is the value of a feature map after activation function. There are multiple types, like, Max, Sum or Average, however the most common and preferred one is max-pooling. In max-pooling it is defined a spatial neighborhood and gets the max unit from the feature map based on that filter dimension that can be, for example, a 2×2 window. Fig. 3.3 shows an example of max-pooling operation, with a 2×2 window and stride of 2 taking the maximum of each region reducing the dimensionality of the Feature Map.

**Fully Connected Layer**

Being one of the latest layers of a CNN, coming right before the output layer, the Fully Connected layer (FC) works like a regular Neural Network at the end of the convolutional and pooling layers. Every neuron from the layer before the FC layer is connected to every neuron on the fully connected one. The FC Layer purposes is to use the output features from the previous layer (that can be a convolution or a pooling layer) and classify the image based on the training dataset. Basically, the fully connected layers of a CNN behave as a classifier with convolutional layers outputs as the classifiers input.

**Training**

To achieve low error rates, it is recommended that a CNN is trained on a massive database of images. Backpropagation is used to train the CNN by calculating a gradient that is needed in the updating of the weights in the network. To train the CNN there are a few different steps depending on which layer that is being trained. Fig. 3.4 shows an example of object detection and classification convolution neural network.

In shipyards, various CNN application technologies are being developed for vision-based object recognition. Fig. 3.5 is the case of using CNN for machine diagnosis. This is a case where the vibration signal of an electrical motor is imaged as a spectrogram and the types of failure are classified using CNN. The CNN method showed higher performance than the conventional machine learning methods. Fig. 3.6 shows the case of using CNN for fire monitoring in the engine room of a ship. Although the fire monitoring sensor array is installed on the ceiling of the engine room, there is a problem that it takes up to 5 minutes or more for smoke to be detected by the sensor when a fire occurs. It was possible to detect a fire in real time based on CNN using smoke images in the engine room. The last case using CNN is shown in Fig. 3.7, it is an obstacle detection technology for autonomous navigation. There are traditional sensors such as radar and AIS on ships, but obstacles that cannot be detected by existing sensors are detected by

CNN using camera images. In addition, for quality inspection and safety monitoring, CNN is being widely applied in shipyards.

## 3.2. Data generation using mode superposition

A large amount of data is required to develop a deep learning-based VIV detection algorithm. As the amount of VIV data that can be obtained by measuring an actual ship or through systems analysis is greatly limited, we thought that it would be difficult to obtain the data required for deep learning with data augmentation technology. For this reason, we simulated a VIV phenomenon and utilized the result as training data. A 3D fluid-structure interaction analysis of a propeller is problematic in that the analysis would take a long time. Accordingly, we propose a method of generating a large amount of data by creating a vibration model based on the modal-superposition method that produces a result similar to that of a fluid-structure interaction analysis. In summary, the method is as follows:

**Training data generation process**

1. Natural frequencies and mode shapes are randomly generated to simulate the vibration characteristics of diverse ships.
2. Natural frequencies and mode shapes of underwater structures are also randomly generated.
3. The excitation force of the RPM order component is applied to simulate the excitation force of the main engine and the propeller. The magnitudes of the excitations are set to proportional to RPM. The phases of the excitations are

randomly set.

4. The excitation force at a constant frequency is applied to simulate the excitation forces of the auxiliary machines. On/off is randomly set. The magnitudes and phases of the excitations are randomly set.
5. The occurrence of lock-in is randomly set. (There is a case in the learning data in which no VIV occurs.)
6. The range of RPM and the strength of the excitation force at the time at which lock-in occurs are randomly set.
7. Measurement noise is taken into account.

**Calculation process**

1. A system matrix [H] is constructed from the randomly generated mode characteristics.
2. An excitation vector {F} is organized from the information about the main excitation force of the ship, the excitation forces of the auxiliary machines, and the excitation forces of the underwater structure.
3. Calculation of the vibration velocity response and conversion to a time signal is carried out and noise is taken into account; $\{V\}=j\omega[H]\{F\}$ and $v(t)=|V|\ \cos(\omega t+\varphi)+n(t)$ where $j=\sqrt{(-1)}$.
4. The linear spectrum of the v(t) signal is calculated for each RPM.

5. A waterfall chart (1 set) is generated for one ship by accumulating the spectrum at different RPMs.
6. RPM range: 1 rpm steps from 21 – 80 rpm (60 points along the RPM axis)
7. Frequency range: 0.125 Hz steps from 0.125 – 100 Hz (800 points along the frequency axis)
8. A waterfall chart of 60 x 800 size is generated.
9. Data on several ships are generated by repeating steps 1 to 5.

In this study, the number of grids is 60X800, and there is a problem that the number of horizontal grids is too small compared to vertical. In other words, it means that the rpm resolution is lower than the frequency resolution. This is because it is necessary to measure the steady vibration in order to sufficiently express the lock-in phenomenon caused by the vortex deviation, so it is measured and stored for 1 minute or more at each operation speed. to be. In other words, during the test operation of the ship, the vibration is measured by sweeping the rotation speed of the ship's main engine at 1 rpm intervals. In order to increase the RPM resolution, it is possible to obtain a spectrogram from the continuously measured signal, but empirically, the signal obtained through the quick bypass operation is often lower in magnitude than the vibration value measured at 1 rpm intervals. There is a method that can measure vibration while driving at an rpm

interval that is finer than 1 rpm interval, but it is judged that it is difficult to apply from a practical point of view. Finally, in this study, the number of grids was decided to be 60X800.

Though a waterfall chart generated through a simplified model is not the result of a fluid-structure interaction analysis, it seems to properly simulate the characteristics of an empirically observed waterfall chart. The above process is used to generate 10k training sets for parameter learning, 1k validation sets are used for hyper-parameter tuning, and 1k test sets are used for the final performance evaluation. The data generated are shown in Fig. 3.8. The X data are waterfall chart as the input data, and Y data are utilized as the label data for supervised learning, showing the frequency and RPM at which lock-in occurs. The value of Y at the RPM and frequency where lock-in occurs is 1; it is 0 in any other case. During the learning process, the lock-in frequencies and RPMs marked as 0 and 1 will be converted to the parameters of the bounding box.

## 3.3. Structure of the proposed CNN model

An algorithm was developed that can detect VIV from waterfall charts based on CNN-based object detection technique. Though the object detection algorithms currently used for image recognition technology classify objects that have been detected, in this study, as the purpose is to detect only the lock-in phenomena, a classification function is not required. To train VIV detection algorithm, the loss function of the bounding parameters was utilized and accuracy was assessed using intersection of union (IoU). The bounding box which is rectangle can be parameterized with two central coordinates, height and width. In an object detection algorithm, 2D data are divided into several grids and the probability that the center of the bounding box can be found inside each grid is denoted Pc. The center of the bounding box inside a grid for which Pc = 1 is expressed with a value between 0 and 1; in this study, this value is expressed as Br (center coordinate along RPM axis within a grid cell) and Bf (center coordinate along frequency axis within a grid cell). The rpm range of the bounding box is defined as Rr along overall RPM axis and has a value between 0 and 1. Each parameter is shown in Fig. 3.9. A VIV detector that accepts waterfall charts as inputs produces bounding box parameters Pc, Br, Bf, and Rr as outputs.

The IoU concept cannot be yet applied because a bounding box is not a rectangle, but a straight line with no area. Accordingly, a range (Rf) must also be

set for the frequency axis. In this study, this value is set as a constant ±1 Hz. For such a bounding box, the IoU with the bounding box which corresponds to the ground truth is calculated. The definition of IoU is shown in Fig. 3.10. When it is accurately identified, it has a value of 1, and if there is no overlap, it has a value of 0. In this study, performance is evaluated based on IoU = 0.5. That is, the inference bounding box is judge to be correct when IoU is higher than 0.5.

The pseudo-code of the loss function for learning is shown in Fig. 3.11. The basic structure of the loss function is the square error for the parameters of the bounding box. If no bounding box center is inside a grid cell, the errors for Br, Bf, and Rr are not reflected in the loss function calculation and the algorithm is taught that only the value of Pc is 0. If a bounding box center exists inside a grid cell, the algorithm is taught that Pc is 1 and Br, Bf, and Rr are their true values.

In this study, a waterfall chart with a size of 60 x 800 is divided into 30 x 50 grid cells. That is to say, one waterfall chart has 1,500 grids. For the waterfall charts in which VIV exists among the learning data, the algorithm should learn that the Pc values of 1,499 of the 1,500 grids are 0, and that of only one grid is 1. Learning may be difficult as the loss function does not change significantly even when the algorithm learns that Pc is 0 in all grid cells. In consideration of this problem, the ratio of the number of grid cells where no bounding box center exists, n0, to the number of the grids where a bounding box center exists, n1, is balanced

from 1,499:1 to 1:1. In an object detection algorithm, a weight (Lcoord or Lnoobj) is applied to the cases where a bounding box exists inside a grid and to the cases where no center exists, respectively. In this study, a trial-and-error process identified Lcoord = 1 and Lnoobj = 10 as appropriate values.

## 3.4. Deep neural networks

Networks that have been widely used for object detection problems recently, such as SSD and YOLO, show excellent performance in mapping general images, but since the problem in this paper is relatively simple, we tried to use a simple CNN as much as possible. In the case of judging voice signals or diagnosing machine failures using spectrogram, a simple network is used as much as possible and the method of increasing the convolution layers one by one is generally used as needed. However, since this paper is the first research case in which a deep learning methodology is applied for VIV exploration, the network has room for optimization. In the future, if measured data from actual ships are accumulated, follow-up studies are required. We subjected 15 models to the learning process while changing the hyperparameters. The performance of the model presented in Fig. 3.12 was found to be superior to the others. Fig. 3.13 ~ Fig. 3.14 shows the deep learning model created using Tensorboard and the monitoring results of the weight change. A brief explanation of the relevant model is as follows: The input data are 2D data, the waterfall charts, of single channel with a size of 60 x 800 are input without being converted into images. In the meantime, as the vibration level may appear to be very low or very high, pre-processing is applied to the input data using a log function to make big values small and small values big, and then the data are normalized so that all values lie between 0 and 1. The hidden layers are

comprised of only convolution layers and the activation function is an ELU (Exponential Linear Unit) function. The type of activation functions was considered as one of the hyperparameters during the development of VIV detection algorithm. In this study it was found that the accuracy became lower as ReLU (Rectified Linear Unit) function was utilized although ReLU function has been typically utilized for image recognition network models. The size of the input data, 60 x 800, is gradually reduced by applying max pooling so that the final output data are 30 x 50 in size. The size, 30 x 50, is the same as the size of the grid mentioned earlier. As the output layer should output the parameters of the bounding box (Pc, Br, Bf, and Rr for each of 30 x 50 grid cells), the output data are set to consist of 4 channels with a size of 30 x 50. As the output values of Pc, Br, Bf, and Rr should be between 0 and 1, a sigmoid function that produces values between 0 and 1 is used as the activation function of output layer. There may be multiple lock-in's for a waterfall chart; it means that Pc values are 1 for the many grid cells. Considering the sum of output values from softmax function is always 1 while the output values from sigmoid function is between 0 and 1 at each node, sigmoid function is more desirable for the calculation of Pc. Rf is introduced only for evaluation of IoU and does not affect learning. The work of drawing a bounding box on a waterfall chart from the bounding box parameters Pc, Br, Bf, Rr and Rf is done using the post-processing code.

## 3.5. Training and diagnosis steps

The training phase utilized random mini-batches of 100 sets with a dropout rate of 0.1. The loss function value and the accuracy of the VIV detector are shown in Fig. 3.15. The training was stopped before overfitting occurred, which is when the loss function value for the training set is very low but the value for the validation set becomes high. For the inference bounding box, which is used to determine accuracy, the parameters of the bounding box with the maximum Pc value among all Pc values for 30 x 50 grid cells were plotted. The accuracy for the training set is 92%, the accuracy for the validation set is 87%, and the accuracy for the test set is 82%. Model organization and learning were done with Python/Tensorflow, and Tensorboard was used to monitor the learning process [27]. The detailed prediction results for the training, validation and test sets are shown in Table 3.1. The false-positive rate for the test sets was 18.8%, and the false-negative rate was 6.5%. In the case of false-positives, which occur at a relatively high rate, no serious situation arises because the waterfall chart will be closely reviewed by the experts. Although the false-negative rate is relatively low, serious problem may occur in the future because there is no chance for the experts to closely review it. In future work, it is desirable to develop the VIV detection algorithm so that the false negative rate is further lowered.

## 3.6. Performance of the diagnostic model

Typical examples of VIV detection for the test sets are shown in Fig. 3.17~Fig. 3.19. In Fig. 3.17, an explicit lock-in phenomenon is detected, which can even be seen visually, and in Fig. 3.18, a very small lock-in component that is difficult to visually detect is present. In Fig. 3.19, a lock-in phenomenon which looks similar to the vibration component of a ship auxiliary machine is also detected.

The VIV detection system utilized learning data in which no lock-in occurs or lock-in occurs only at one frequency. In some cases of actual ship data, lock-in phenomena occur at many frequencies. Though such a difference may raise concerns that the VIV detector may detect only one lock-in frequency, as the filter of the convolution layer sweeps 2D input data and sends the output to the next layer, it seems that multiple lock-ins can in fact be detected. For actual use of the detection algorithm, the bounding box will be drawn for Pc values higher than a reference Pc value which is empirically defined by user.

**Table 3.1** Detailed prediction results for learning data sets

| Training set (Accuracy = 91.5%) | | | Validation set (Accuracy = 87.3%) | | | Test set (Accuracy = 82.4%) | | |
|---|---|---|---|---|---|---|---|---|
| | Positive | Negative | | Positive | Negative | | Positive | Negative |
| True | 91.4% | 92.1% | True | 86.5% | 94.5% | True | 81.2% | 93.2% |
| False | 8.6% | 7.9% | False | 13.5% | 5.5% | False | 18.8% | 6.8% |

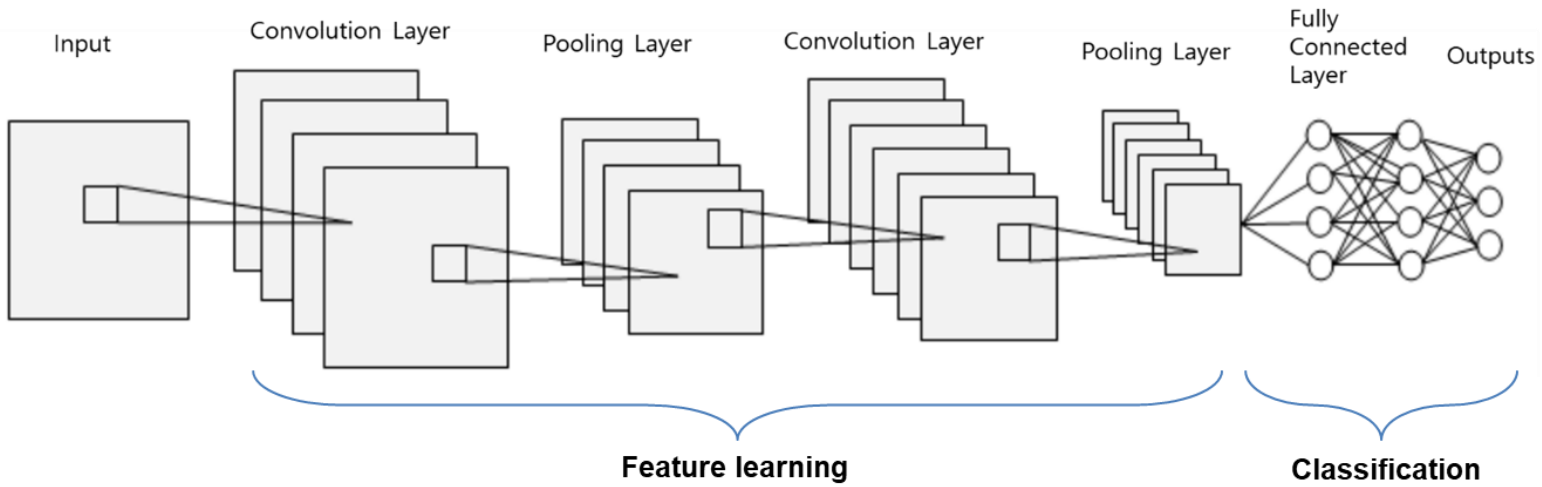


**Fig. 3.1** Typical structure of convolution neural networks

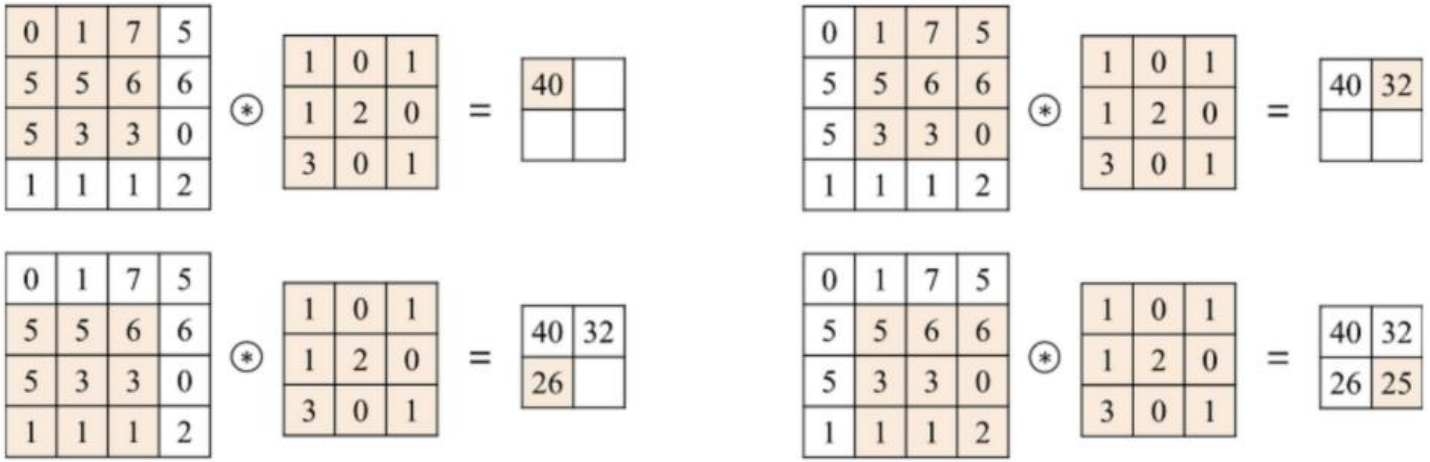


**Fig. 3.2** Example of convolution operation

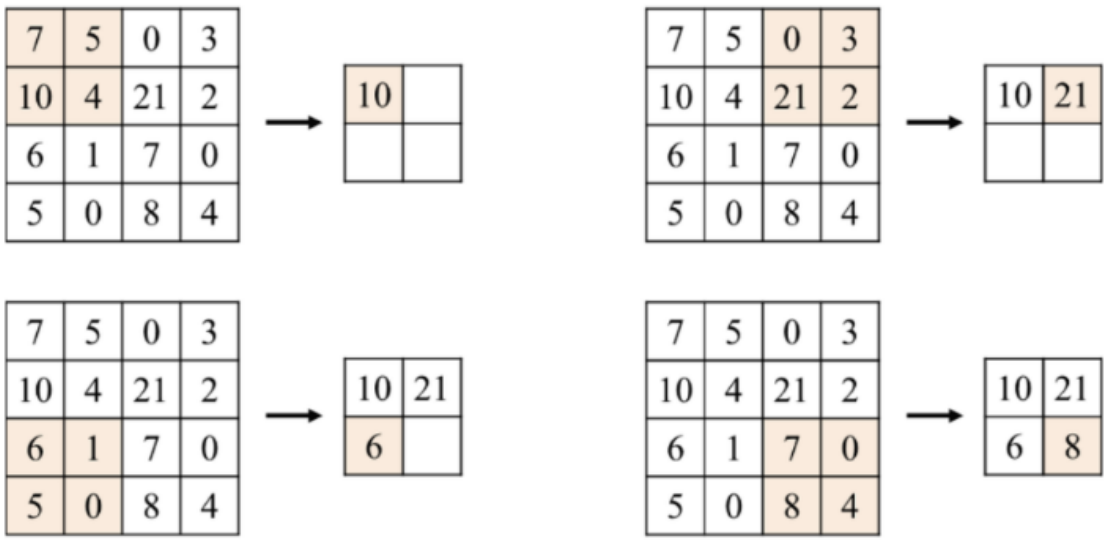


**Fig. 3.3** Example of pooling layer operation(max)

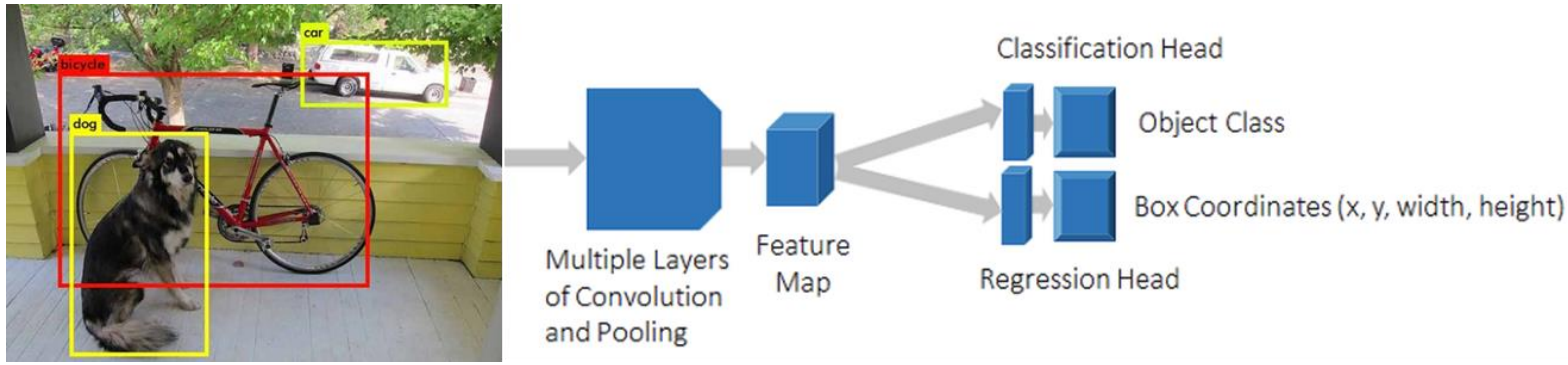


**Fig. 3.4** Example of object detection and classification using CNN

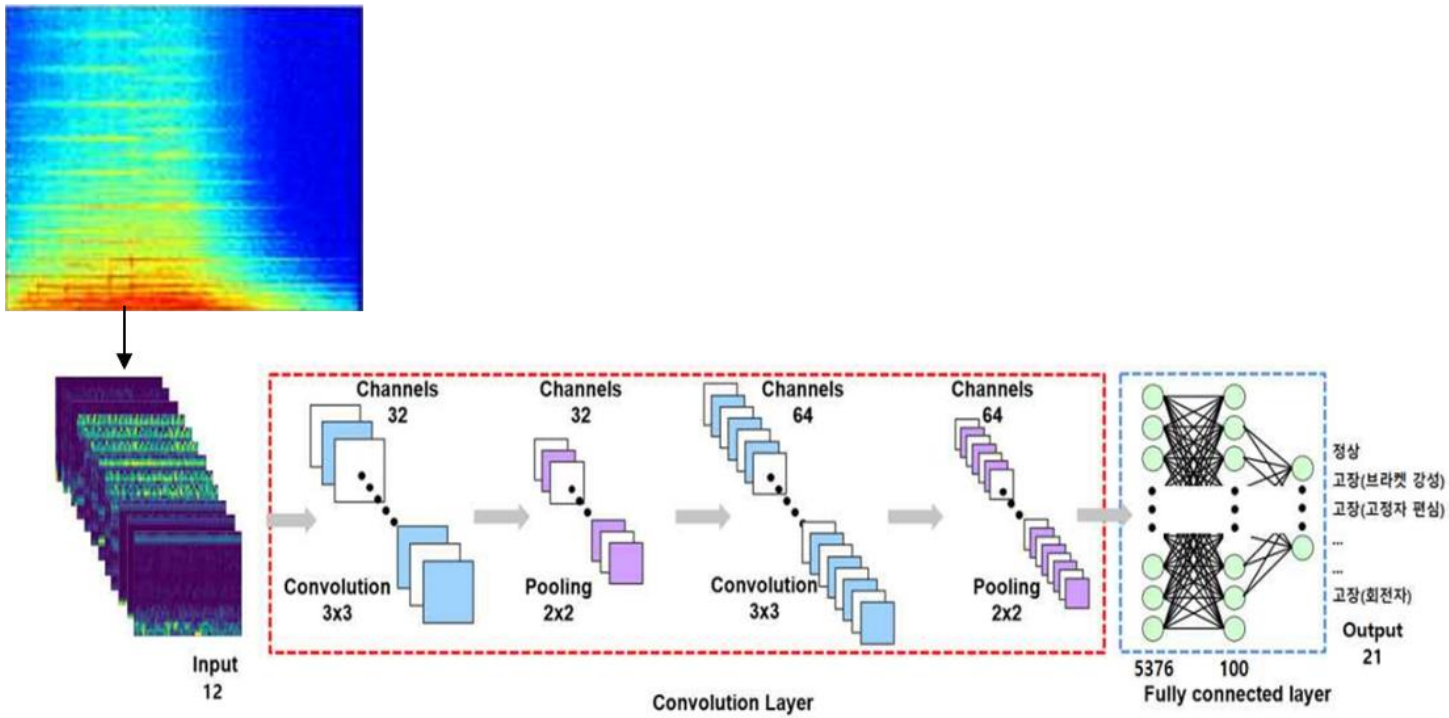


**Fig. 3.5** Example of CNN application in shipyard: diagnosis of electric motor damage using vibration spectrogram

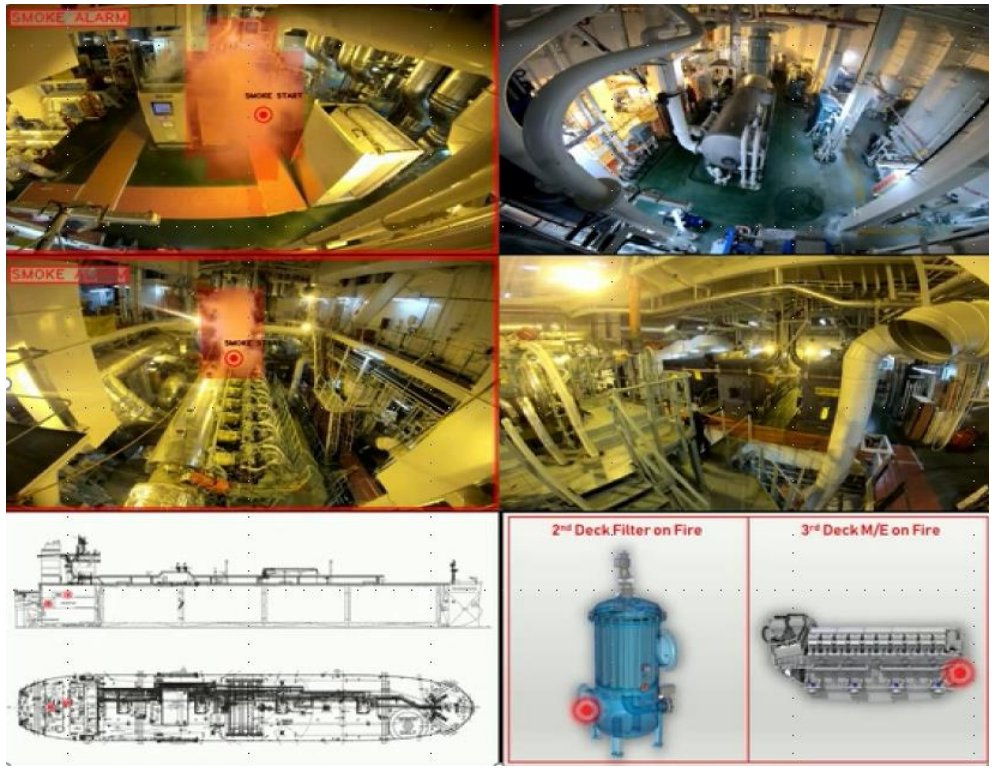


**Fig. 3.6** Example of CNN application in shipyard: image-based engine room smoking detection


**Fig. 3.7** Example of CNN application in shipyard: image-based obstacle detection for ship navigation

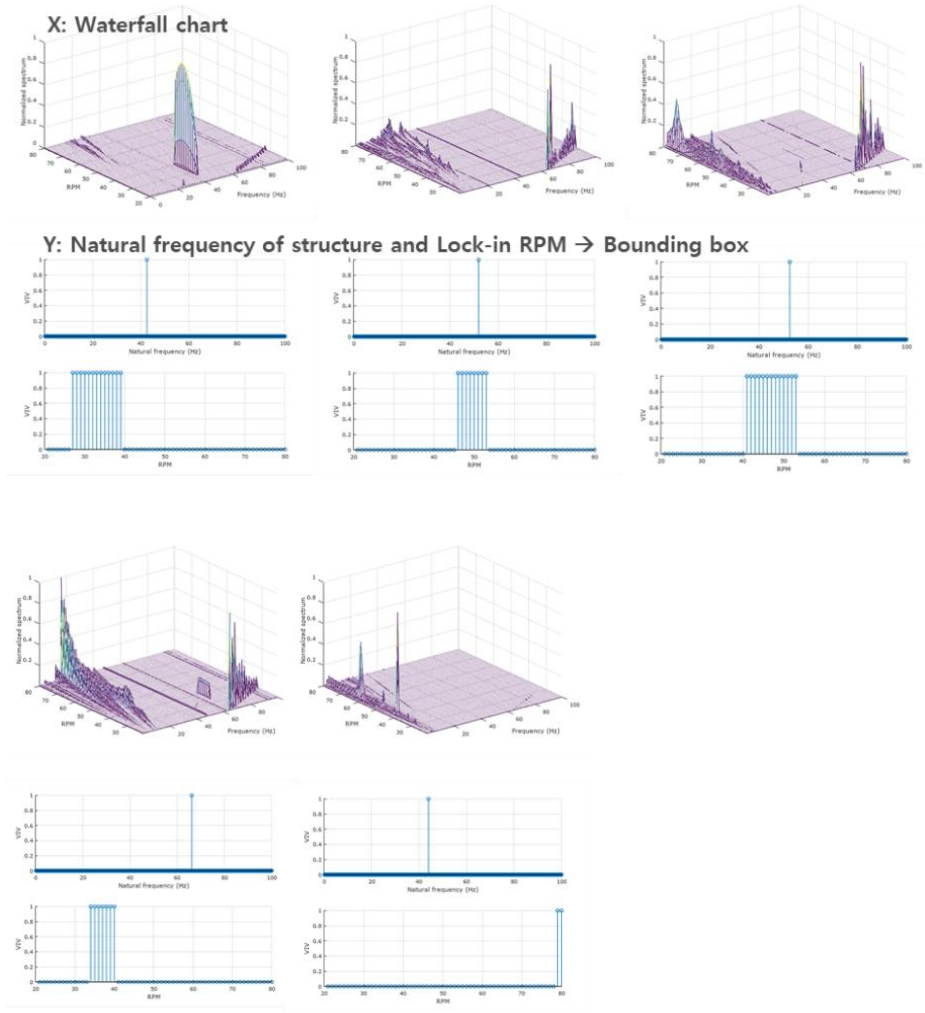


**Fig. 3.8** Examples of generated data sets

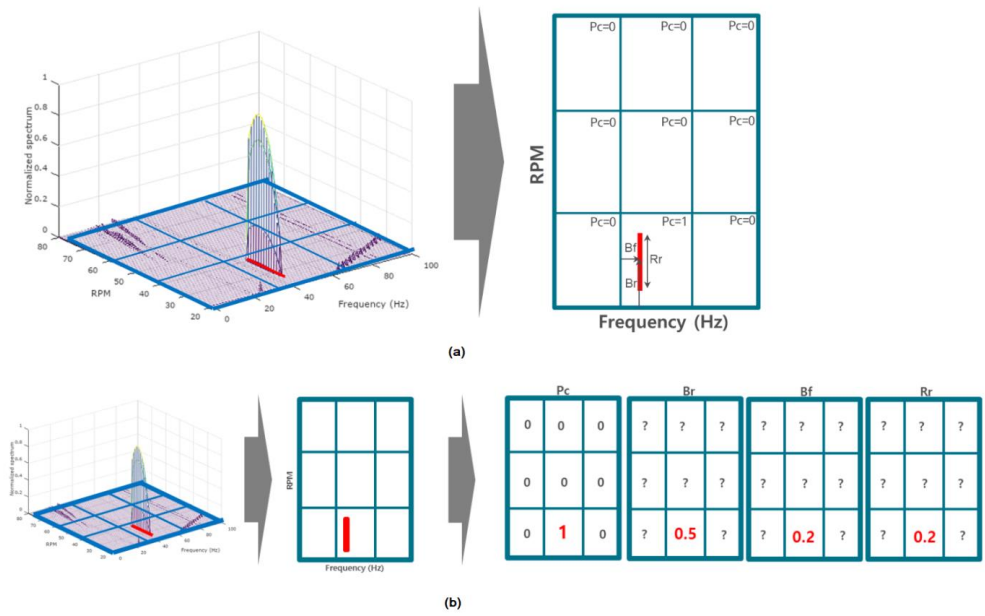


**Fig. 3.9** Bounding box parameters (a) Definition of bounding box parameters;

(b) Data structure of bounding box parameters for training

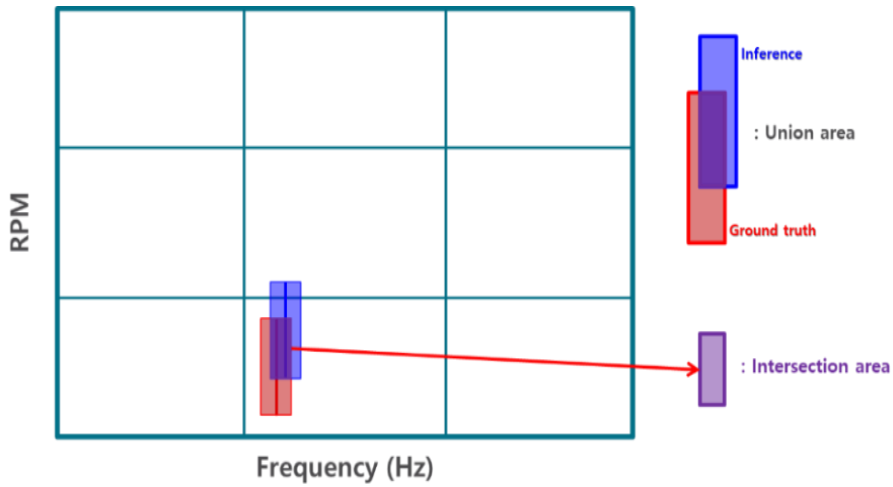


**Fig. 3.10** Definition of intersection of union (IoU)

```
Lcoord = 1.0
Lnoobj = 10.0

Pc2 = sum(Pc_true-Pc_prediction)^2
Br2 = sum(Br_true-Br_prediction)^2
Bf2 = sum(Bf_true-Bf_prediction)^2
Rr2 = sum(Rr_true-Rr_prediction)^2

n0 = sum(1-Pc_true)
n1 = sum(Pc_true)

cost_noobj = (1/n0)*sum( (1-Pc_true)*Lnoobj*(Pc2) )
cost_coord = (1/n1)*sum( Pc_true*(Pc2+Lcoord*(Br2+Bf2+Rr2)) )
cost = 1/2*(cost_noobj+cost_coord)
```

**Fig. 3.11** Pseudo-code of loss function

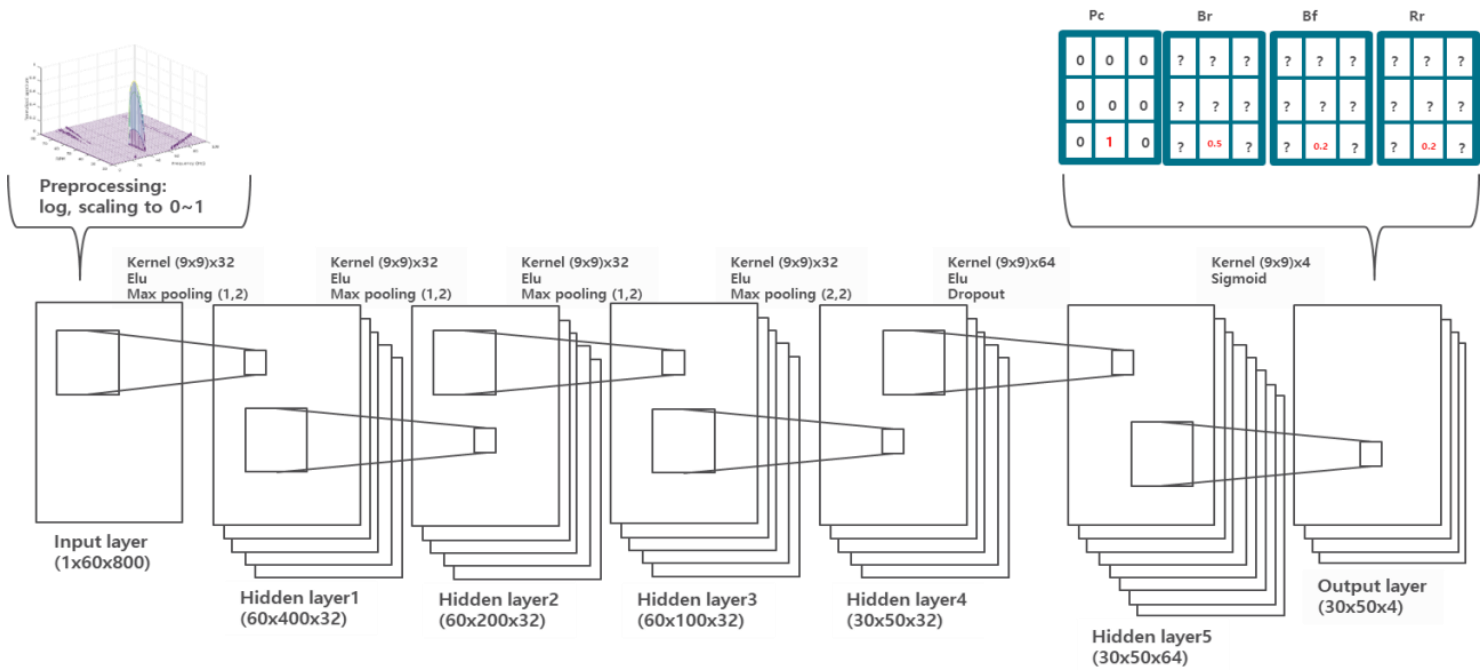


**Fig. 3.12** Deep neural network architecture for VIV detection

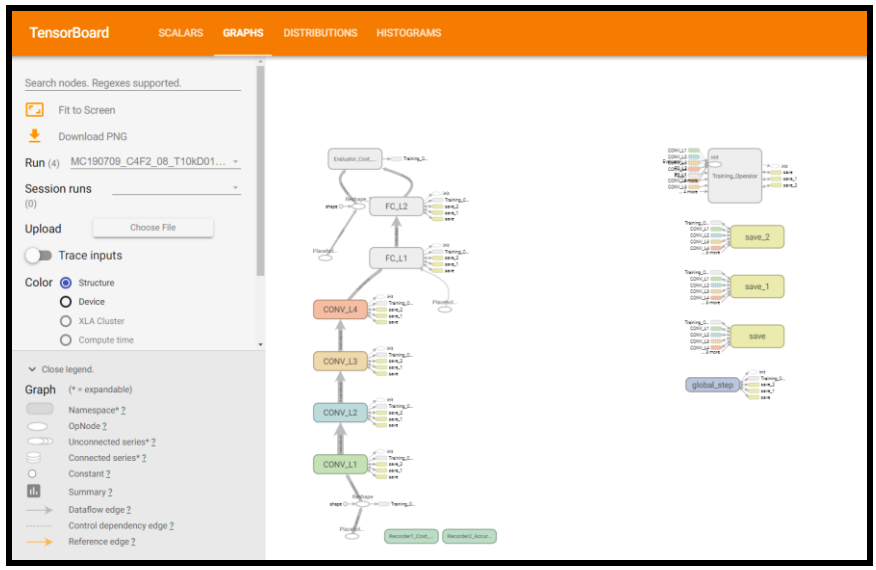


**Fig. 3.13** Development of Neural Network Model Using Tensorboard: A Neural Network Model with 6 Layers

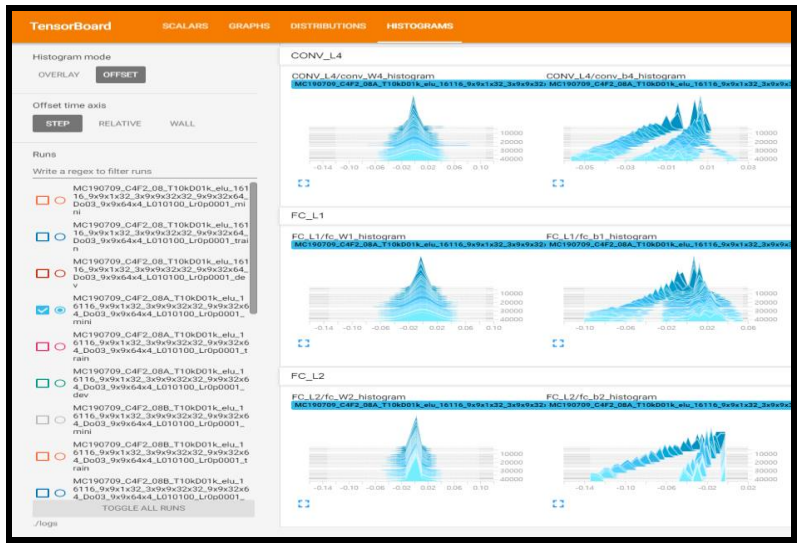


**Fig. 3.14** Monitoring weight change using Tensorboard: Weight (W,b) changes as training progresses

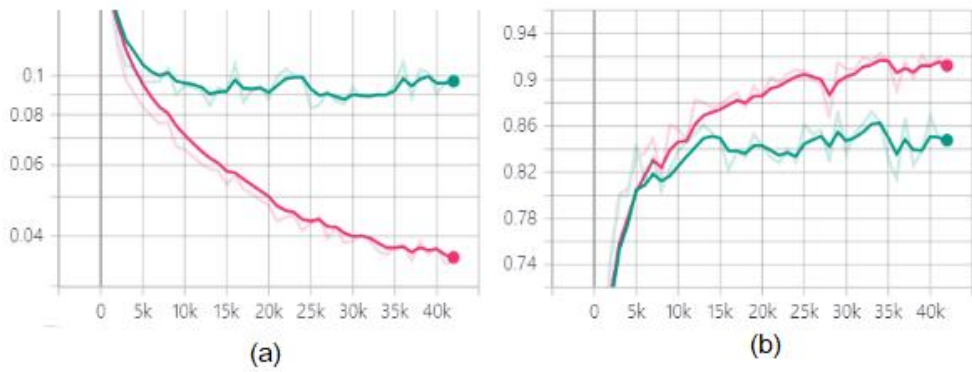


**Fig. 3.15** Loss function and accuracy for the training (magenta) and validation (green) data sets

(a) Loss function; (b) Accuracy

(b)

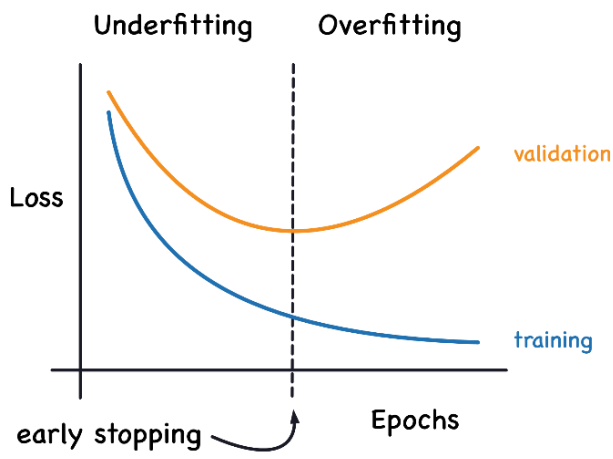


**Fig. 3.16** Validation loss function and overfitting criteria

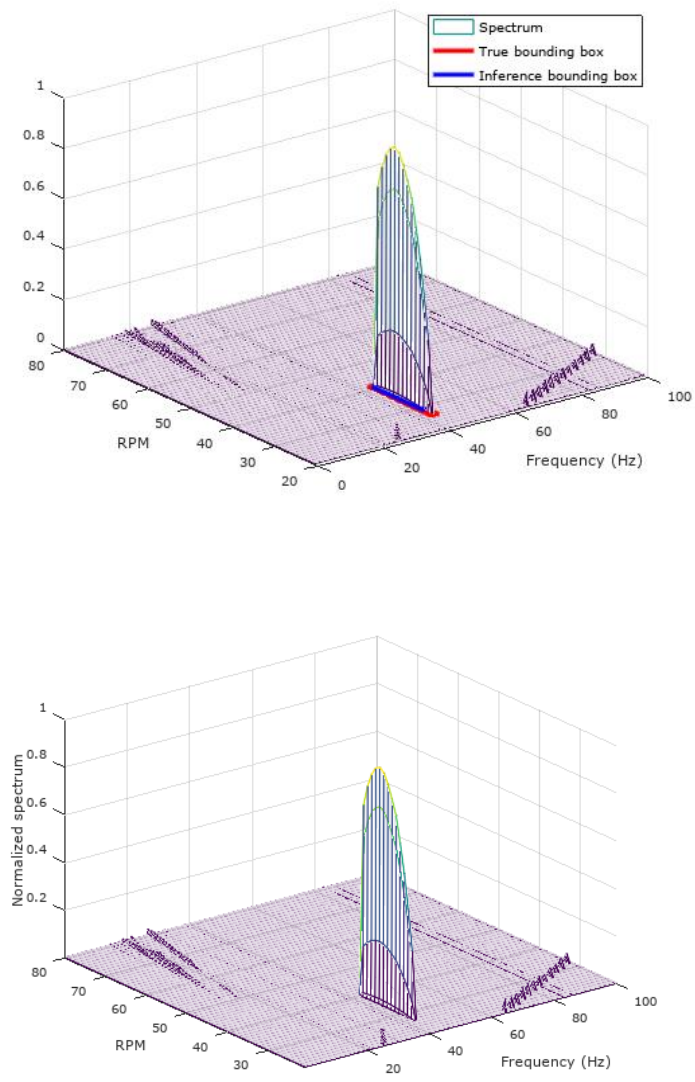


**Fig. 3.17** VIV detection results for the test data set (red box: ground truth; blue box: inference)

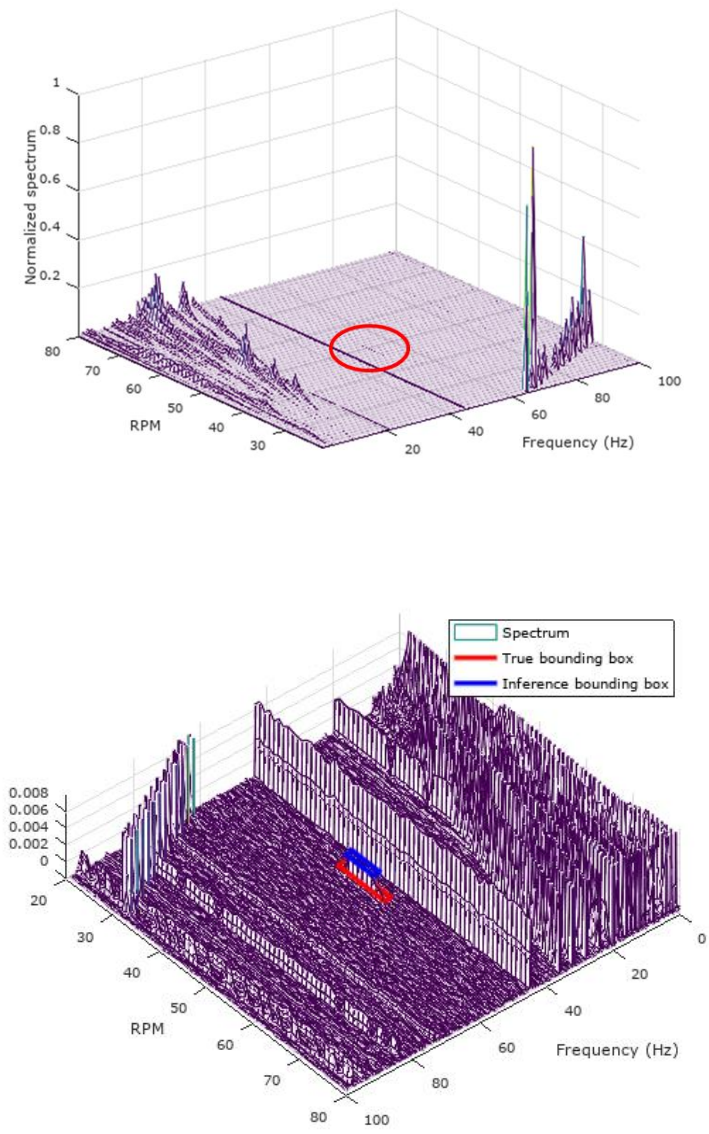


**Fig. 3.18** VIV detection results for the test data set (red box: ground truth; blue box: inference)

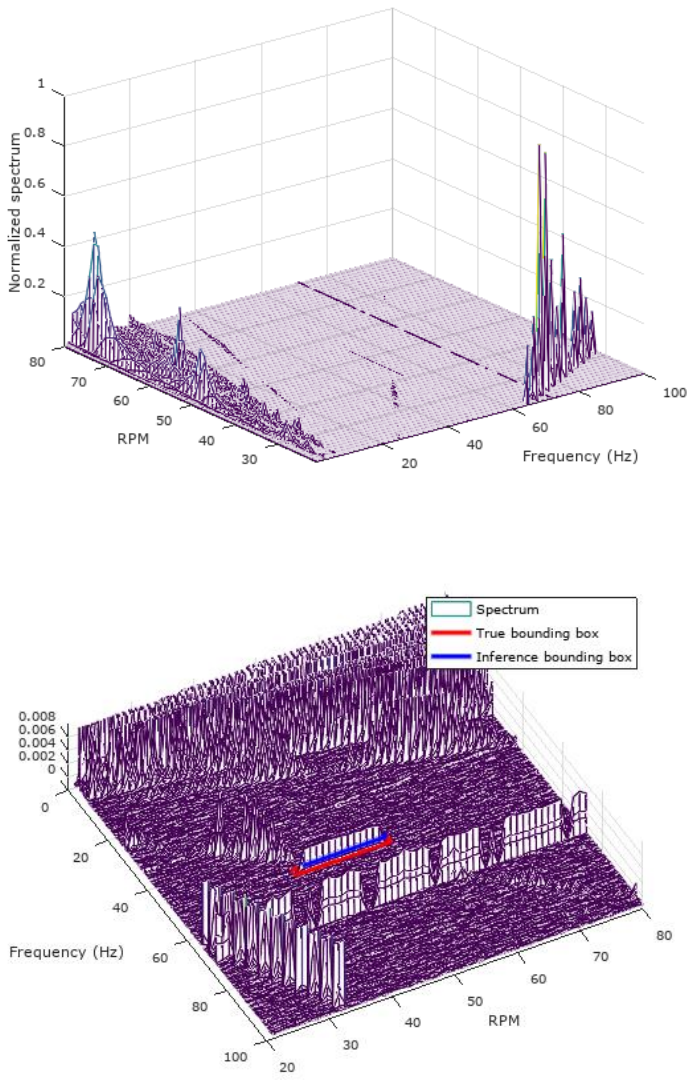


**Fig. 3.19** VIV detection results for the test data set (red box: ground truth; blue box: inference)

# CHAPTER 4.
# EXPERIMENTS AND RESULTS

The VIV detector was developed using learning data generated by simulating only the apparent characteristics of lock-in phenomena, and its performance must be tested by applying a detector developed using actual data, for which the ground truth are known. To this end, substantiation of the developed detector was conducted using a reduced-scale model of a ship propulsion system.

## 4.1. Experimental apparatus and data collection

In the reduced-scale model test device used to reproduce VIV phenomena, the propulsion shafting system of a real ship is simulated, as shown in Fig. 4.1. It is comprised of a motor, reduction gear, shaft, and propeller; the propeller rotates inside a cylindrical water tank. As vortex shedding may be interrupted by unnecessary flow inside the short cylindrical water tank when propeller thrust occurs, the propeller was designed to prevent thrust. The cross-sectional shape of the propeller blade is NACA0009, as shown in Fig. 4.2, and the trailing edge is a blunt edge with a thickness of 3.22 mm. According to data in the literature [28], the vortex shedding frequency for flow velocity is approximately f/U = 60 Hz/m/s, which means that a vortex shedding frequency of 207.6 Hz occurs under the

operational condition of 80 rpm when the diameter of the propeller is taken into account, as shown in Table 4.1. In the meantime, through finite element analysis of one blade, a vibration analysis conducted for a propeller built of an aluminum material under the condition that the propeller is under water showed that the torsional mode is 204 Hz, as shown in Fig. 4.3. Torsional mode is important because it is the vibration mode that is most easily excited by vortex shedding. To summarize the propeller design, it is a design in which 204 Hz vibration occurs under the operational condition of 80 rpm. The reduced-scale model that was produced is shown in Fig. 4.4.

## 4.2. Results and discussion

Given that propeller VIV is readily detectable on the side shell in an actual ship, the vibration of the reduced-scale model is measured using a 3-axis accelerometer located on the wall of the water tank containing the propeller, which corresponds to the side shell. In addition, 3-axis acceleration was installed in the bearing supporting the shaft to determine the vibration transmission path. Fig. 4.5 shows the sensor installation location and sensor orientation. At the bottom of Fig. 4.5, an example of the vibration value measured by each sensor is shown. Data were obtained for a total of 60 operating speeds at intervals of 2 rpm in the range from 42 to 160 rpm with the propeller under water. The spectrum is acquired in 800 lines, and the waterfall chart is acquired with an input size of 60 x 800, which can be input into the VIV detector.

When the vibration value measured at the tank wall and the vibration value measured at the top of the bearing are compared, the frequency component according to the rotation of the propeller is clearly observed in the tank wall, whereas the rotational speed component of the shaft is observed in the bearing, but the propeller component is not observed. it can be seen that It seems that the vibration of the blade was not transmitted to the shaft due to the high impedance of the shaft, and it is considered appropriate to measure the tank wall vibration rather than the bearing vibration for propeller monitoring. This trend can also be

confirmed for real ships.

The waterfall charts acquired as in Fig. 4.6 ~ Fig. 4.8 showed that frequency components other than the integer multiples of the propeller shaft operating speed appear near 80 RPM and 204 Hz. This suggests that torsional mode lock-in phenomena caused by vortex shedding, as intended in the design, appeared. Three similar frequency components occur near 204 Hz, likely because there are three propeller blades that are very similar to each other, though they are not exactly the same. The results of applying the VIV detector to the waterfall charts of the vibration signals acquired from the reduced-scale model are shown in Fig. 4.9 through Fig. 4.11 with reference Pc is 0.9. These results show that bounding boxes are commonly generated at a frequency where lock-in occurs and at the operating rpm. However, bounding boxes also form where no lock-in phenomenon occurs. As they form with no consistency by channel, they can be distinguished from the true bounding boxes for actual lock-in phenomena. In this regard, if a VIV detector is developed in an architecture with waterfall charts of different channels can be input at the same time, the performance is expected to improve.

Fig. 4.12 through Fig. 4.14, the Pc value, which is the probability that the bounding box will be located inside the grid, is displayed next to the bounding box. It means the probability that VIV exists in the grid. In the theoretical model, 0.9 was used as the threshold value, but in the reduced model, it seems that a different

threshold is needed to distinguish it from the operating frequency and resonance of local equipment. Since the Pc value in the lock-in condition is higher than that of other components, it may be helpful in discriminating the actual lock-in phenomenon, but it will be difficult to generalize because the threshold may be different in other measurement conditions.

As shown in Fig. 4.15, the lock-in of the reduced model has a characteristic that the frequency changes slightly depending on the propeller rotation speed, but the data used for training the network model is that the frequency is constant. Since the lock-in frequency of the actual ship data is almost fixed, the training data is configured that way. Although lock-in is reproduced in the reduced model, it tends to be a little different from the lock-in of the actual ship, and accordingly, the detection performance of the network model seems to be slightly lowered. It is presumed that the fluctuation of the lock-in frequency is because the propeller natural frequency is strongly coupled with the vortex due to the low rigidity of the test blade in the scaled model test as shown in Fig. 4.16.

**Table 4.1** Calculated vortex shedding frequency

| **Vortex shedding frequency calculation*** | | | | | | | |
|---|---|---|---|---|---|---|---|
| Description | Coefficient | Hub Radius | Propeller Radius | Radius | Rotation Speed | Flow Velocity | Vortex Shedding |
| Symbol | Cs | r_hub | r_prop | r_hub < r < r_prop | RPM | U | fv |
| Unit | (Hz/(m/s)) | (mm) | (mm) | (mm) | (Rev./Min.) | (m/s) | (Hz) |
| | 60 | 65 | 500 | 500 | 80 | 4.2 | 251.3 |
| | 60 | 65 | 500 | 413 | 80 | 3.5 | **207.6** |
| 1/10 | 60 | 65 | 500 | 326 | 80 | 2.7 | 163.9 |
| scaled | 60 | 65 | 500 | 239 | 80 | 2.0 | 120.1 |
| | 60 | 65 | 500 | 152 | 80 | 1.3 | 76.4 |
| | 60 | 65 | 500 | 65 | 80 | 0.5 | 32.7 |

* Reference: NACA0009 w/ 100 mm cord length, 10 mm maximum thickness, 3.22 t truncated trailing edge

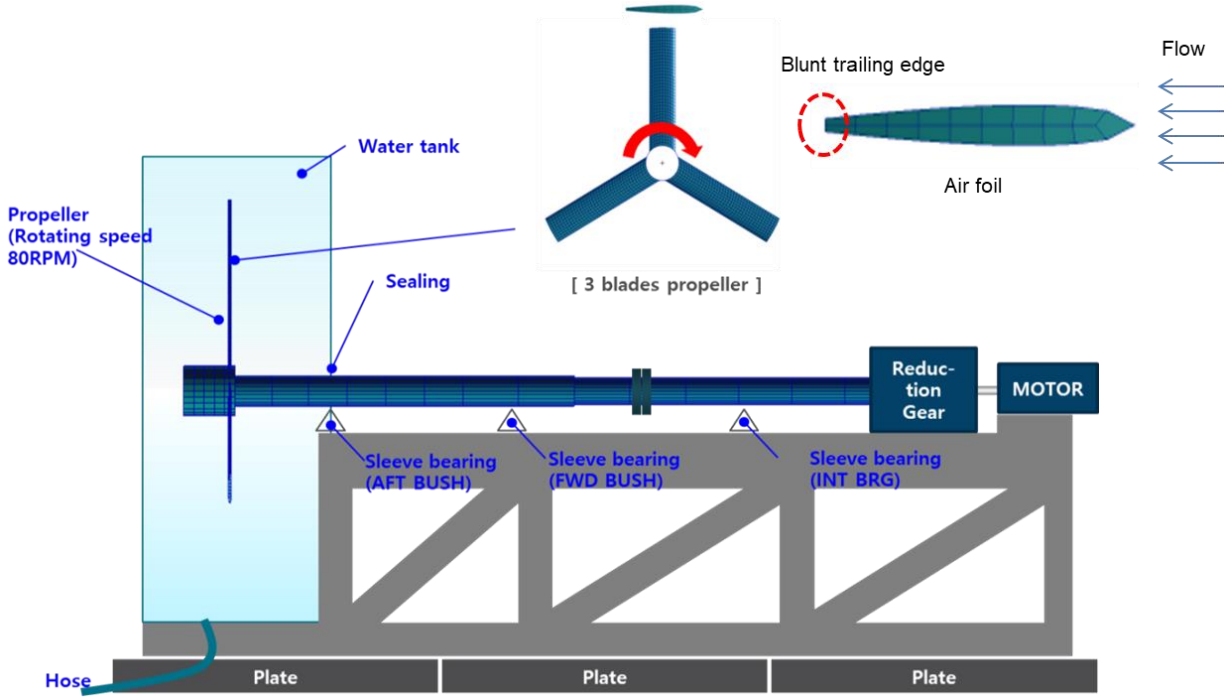


**Fig. 4.1** Schematics of test rig for vortex-induced propeller vibration

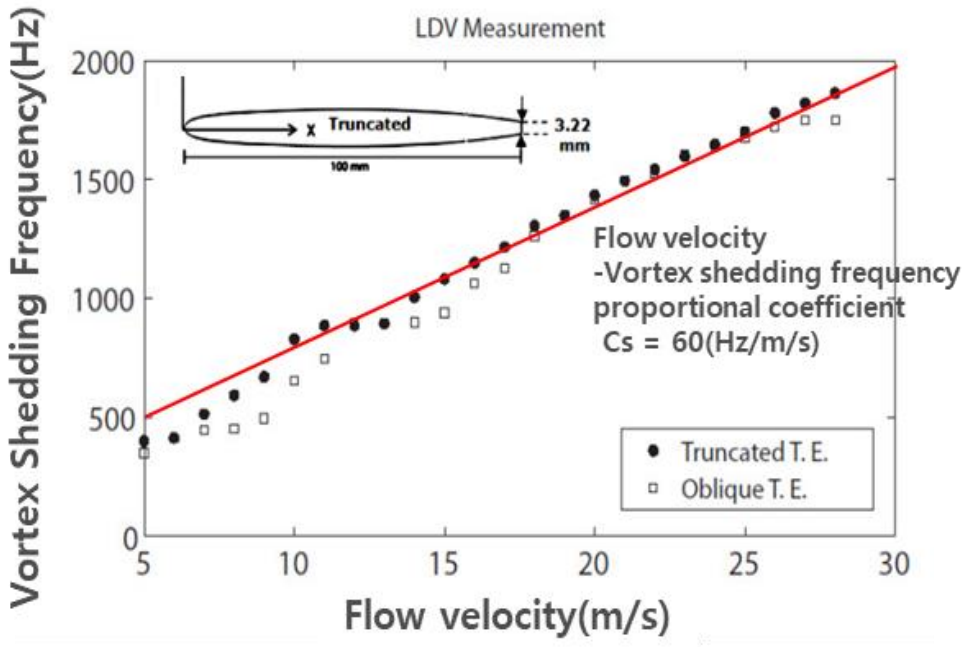


**Fig. 4.2** Selected airfoil and its vortex shedding frequency

**Modal anlaysis results**
***Wet condition, AL Property Utilized**

| 1st nat'l freq. | 2nd nat'l freq. | 3rd nat'l freq. | 4th nat'l freq. | 5th nat'l freq. |
|---|---|---|---|---|
| (Hz) | (Hz) | (Hz) | (Hz) | (Hz) |
| 17.756 | 113.02 | **203.86** | 327.98 | 347.92 |
| 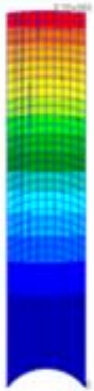 |  |  | 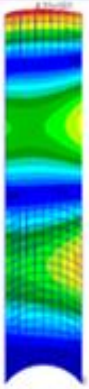 | 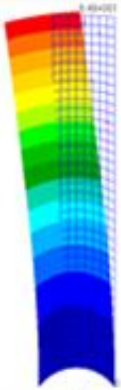 |
| 1st bending | 2nd bending | **1st torsion** | 3rd bending | 1st shear |

**Fig. 4.3** Natural frequency of the designed propeller in water (finite element analysis results)

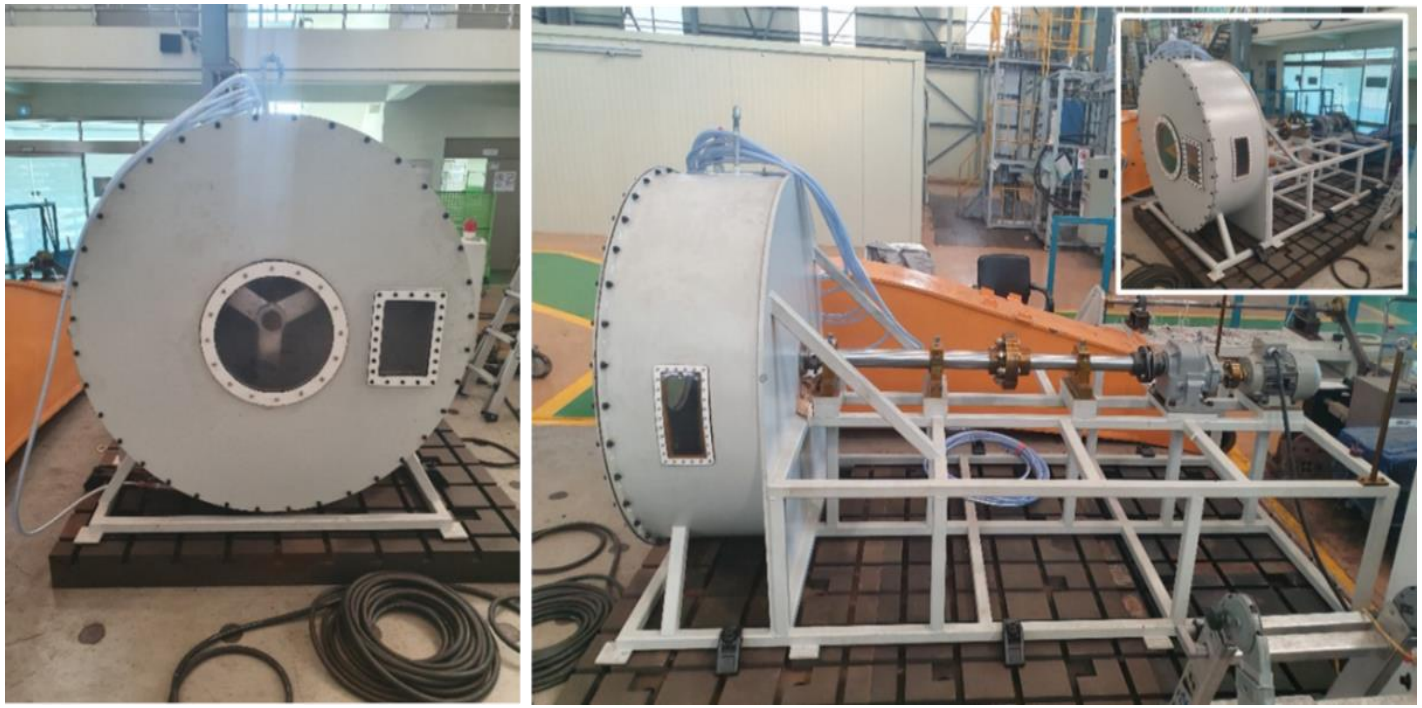

**Fig. 4.4** Test rig for propeller VIV

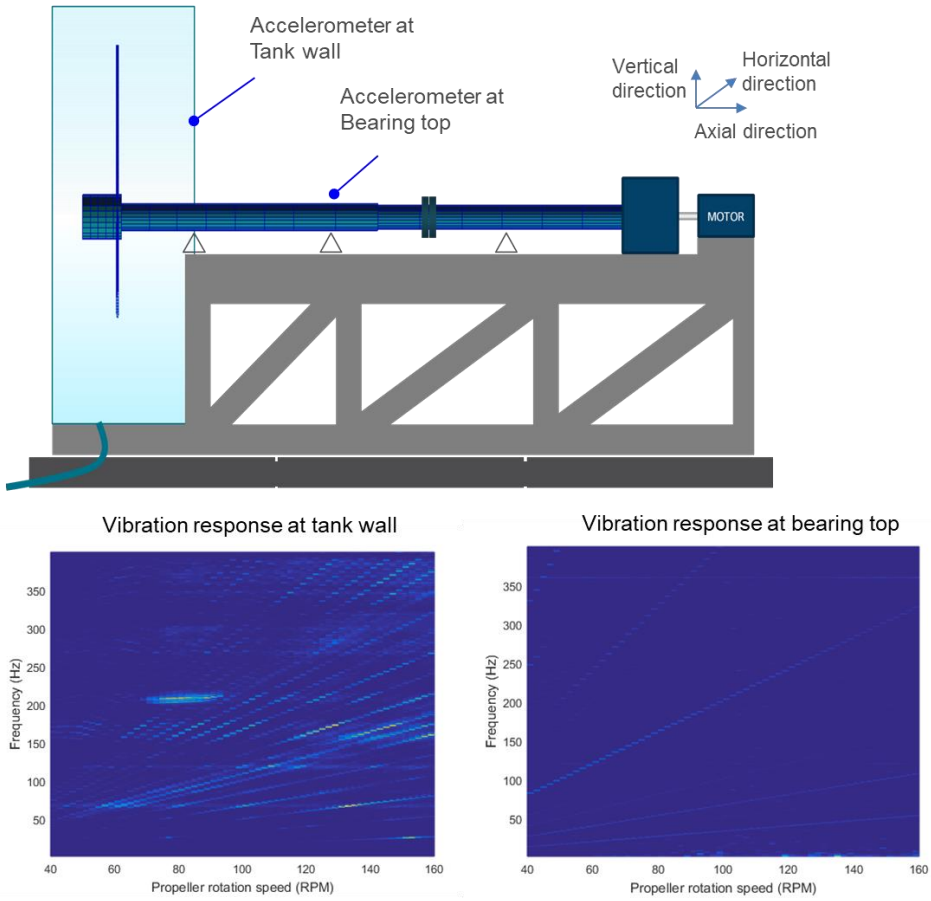


**Fig. 4.5** Measurement position and sensor directions and examples of reduced-scale model test result

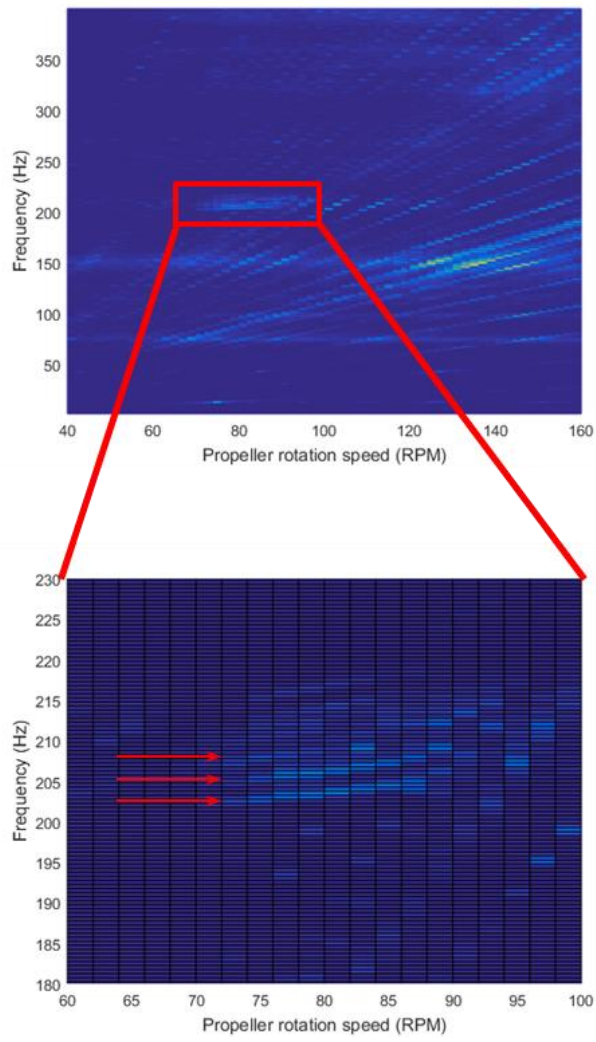


**Fig. 4.6** Vibration measurement data (Horizontal direction) and observed lock-in phenomena

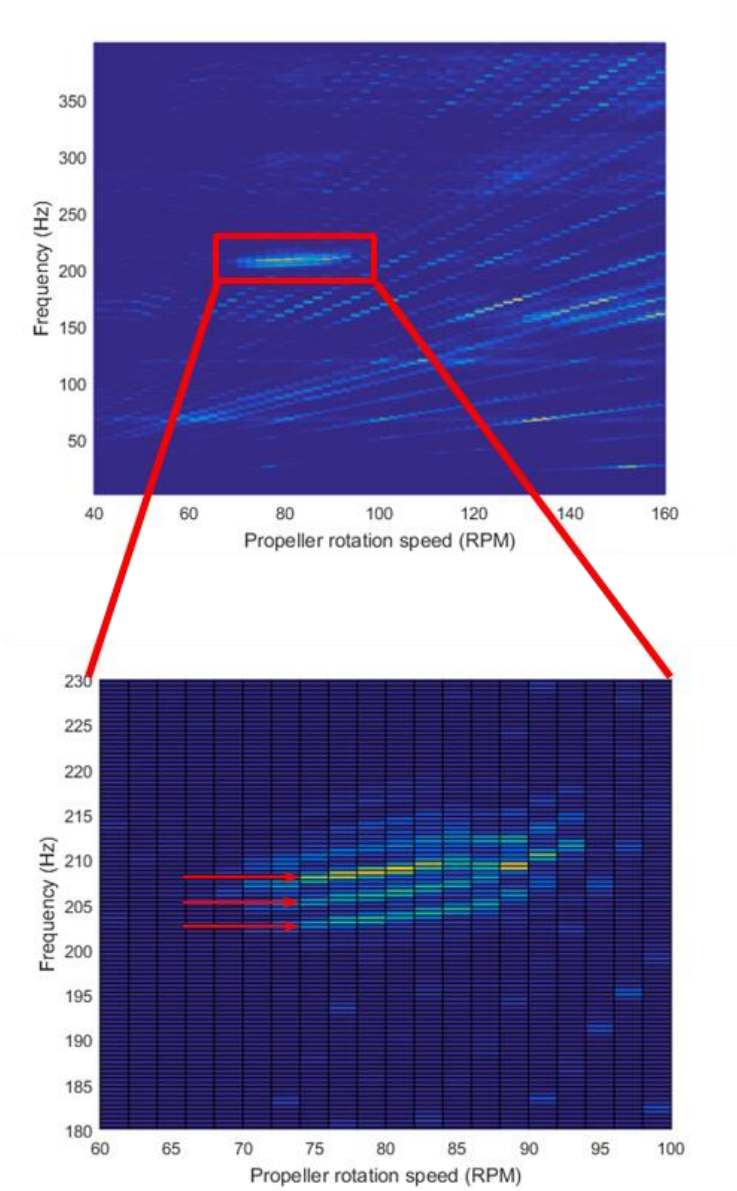


**Fig. 4.7** Vibration measurement data (Axial direction) and observed lock-in phenomena

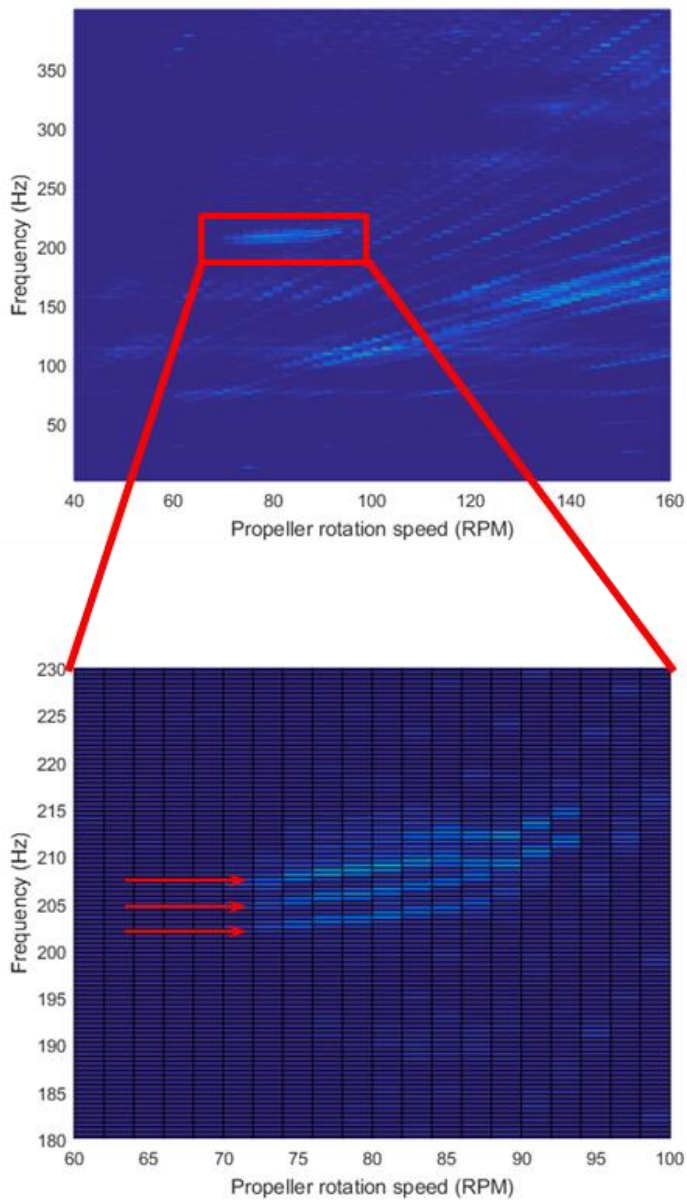


**Fig. 4.8** Vibration measurement data (Vertical direction) and observed lock-in phenomena

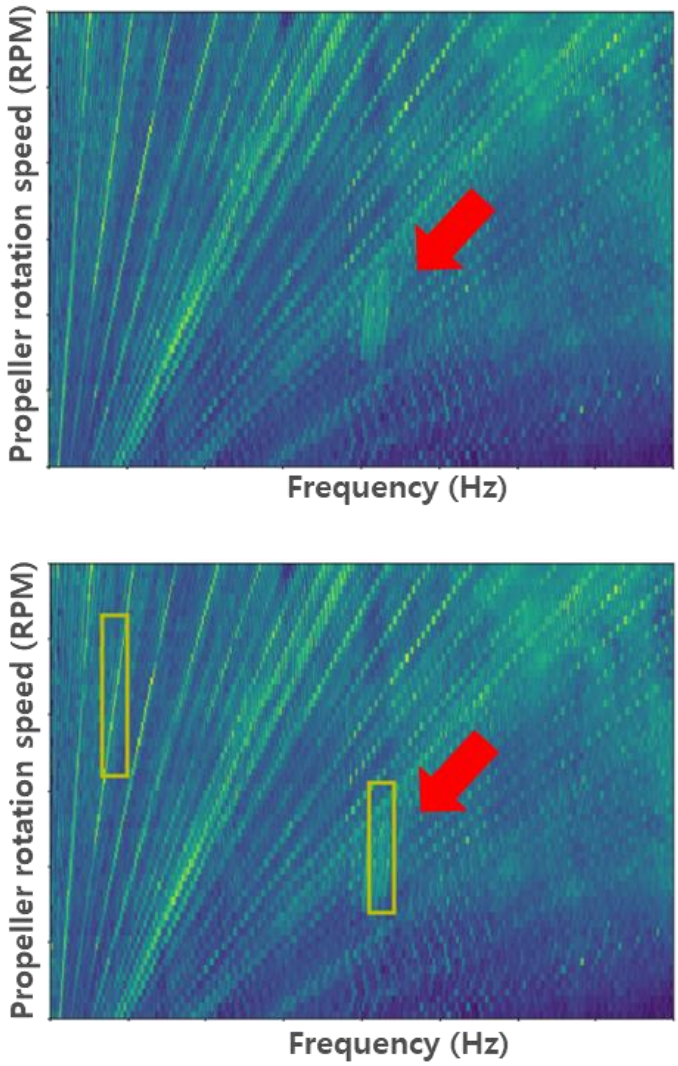


**Fig. 4.9** Results of applying the VIV detection algorithm (Horizontal direction)

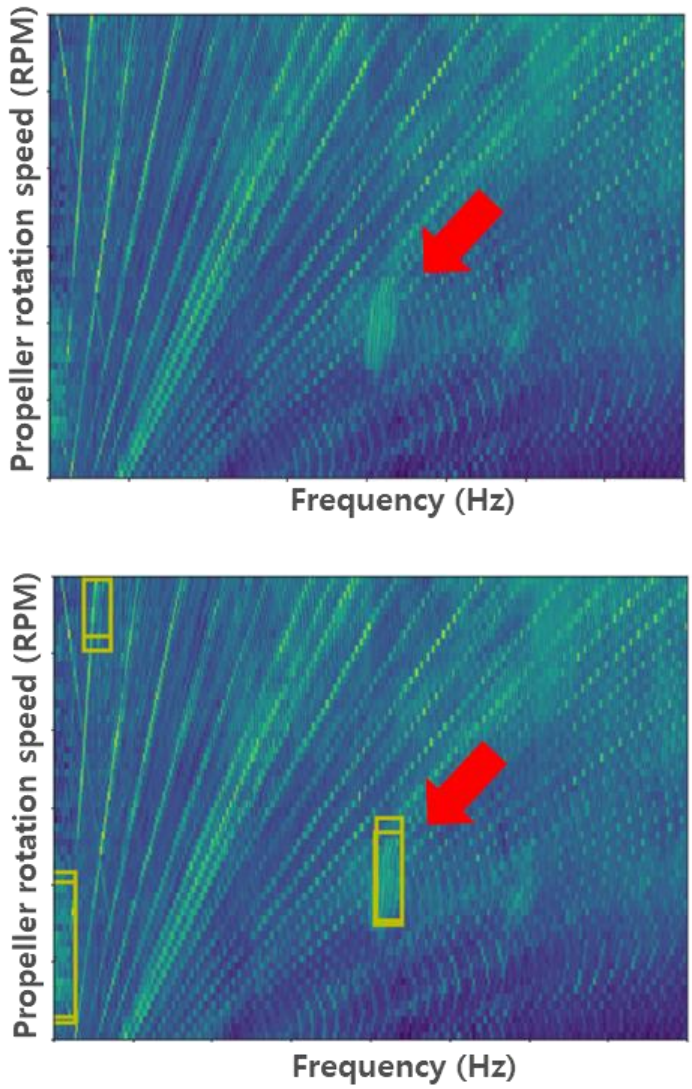


**Fig. 4.10** Results of applying the VIV detection algorithm (Axial direction)

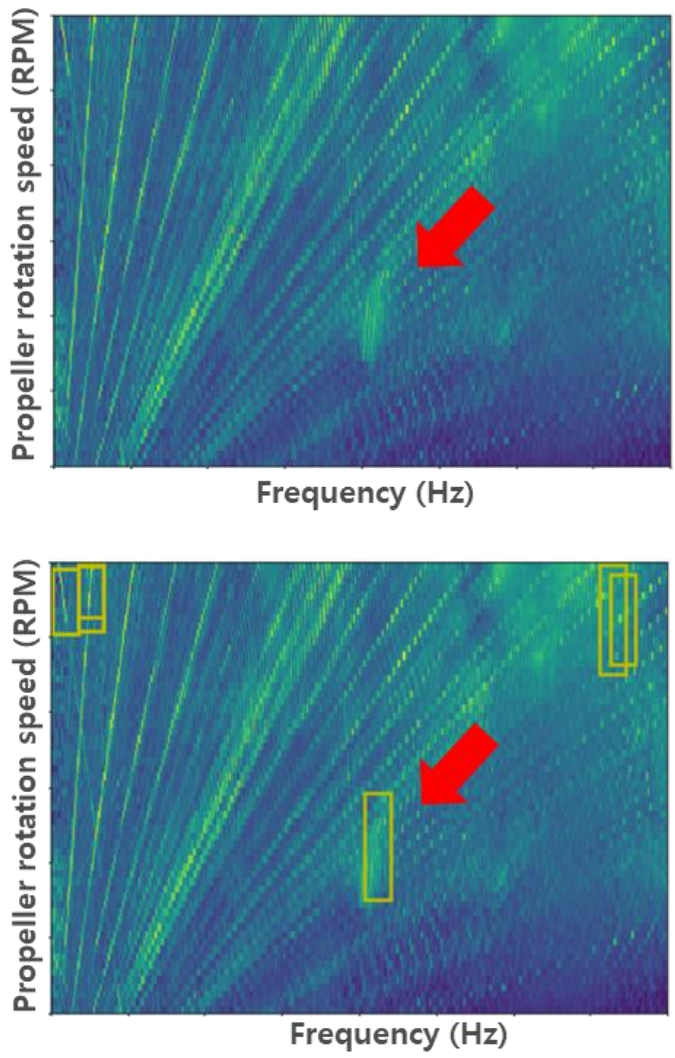


**Fig. 4.11** Results of applying the VIV detection algorithm (Vertical direction)

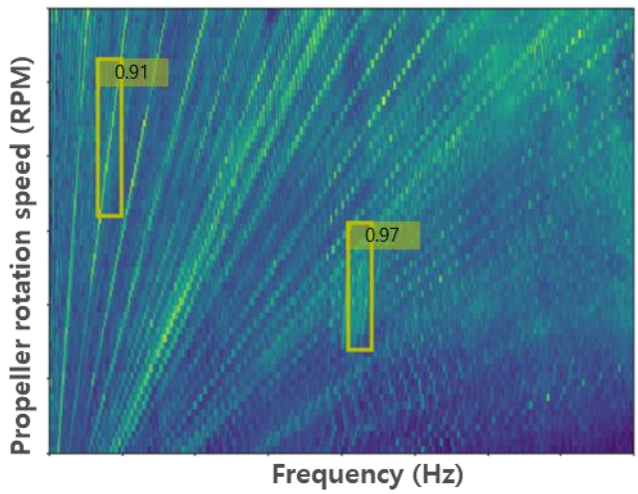


**Fig. 4.12** Bounding box with probability score (Horizontal direction)

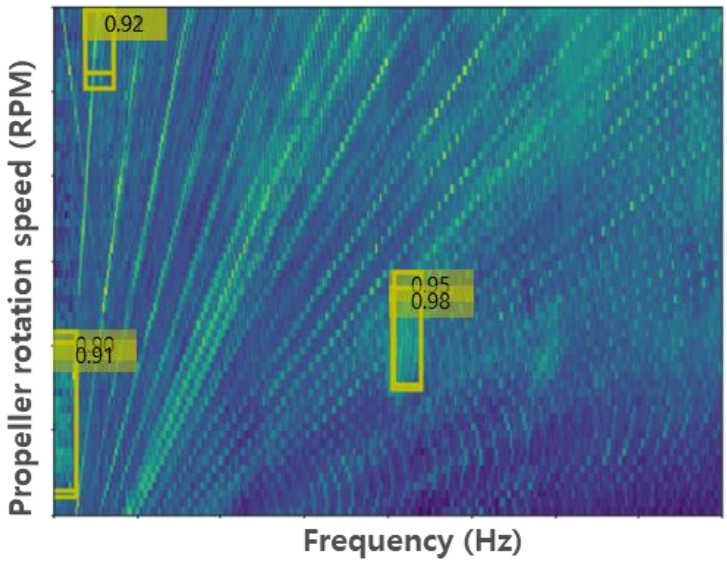


**Fig. 4.13** Bounding box with probability score (Axial direction)

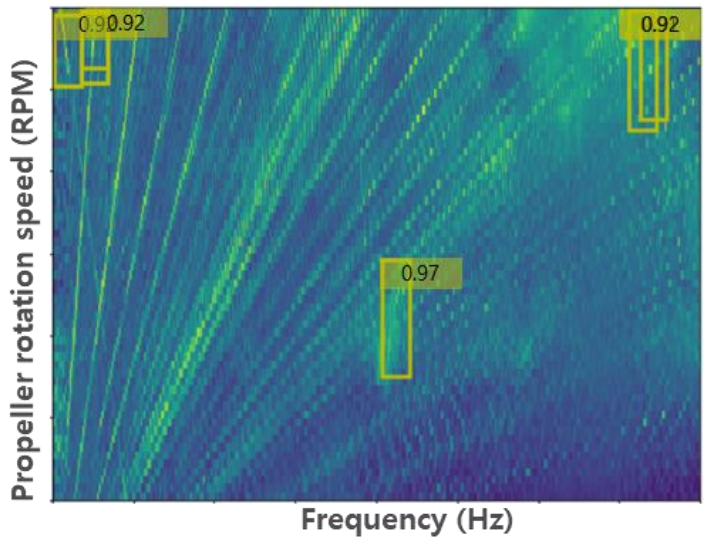


**Fig. 4.14** Bounding box with probability score (Vertical direction)

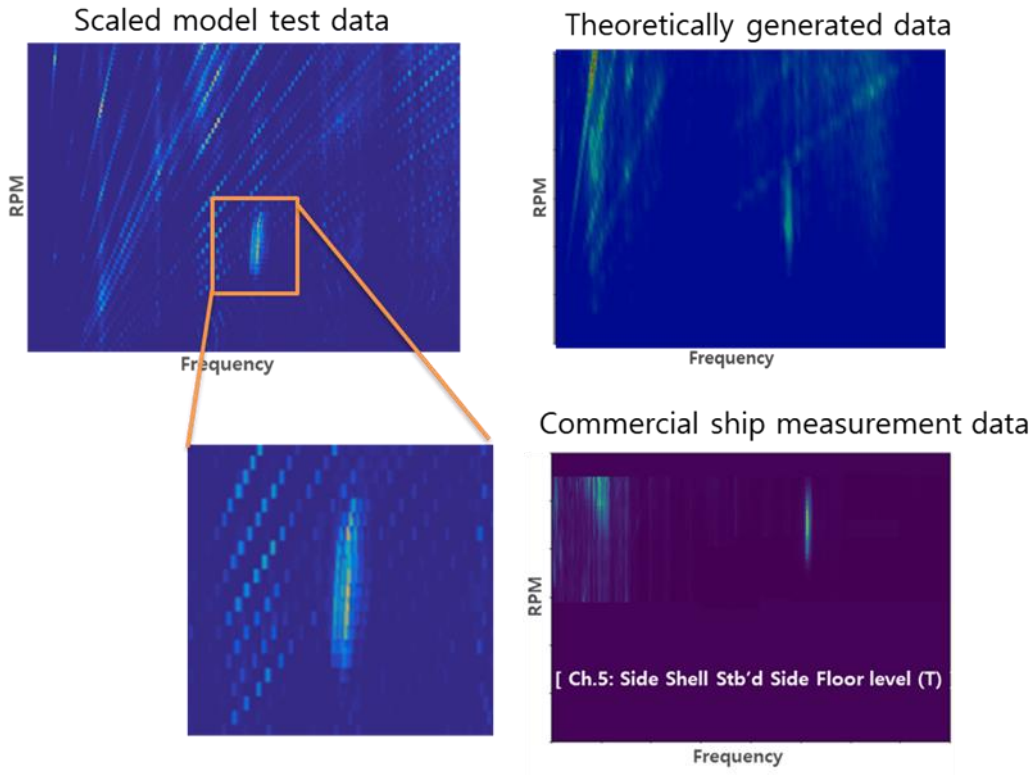


**Fig. 4.15** Comparison of lock-in frequency by data type

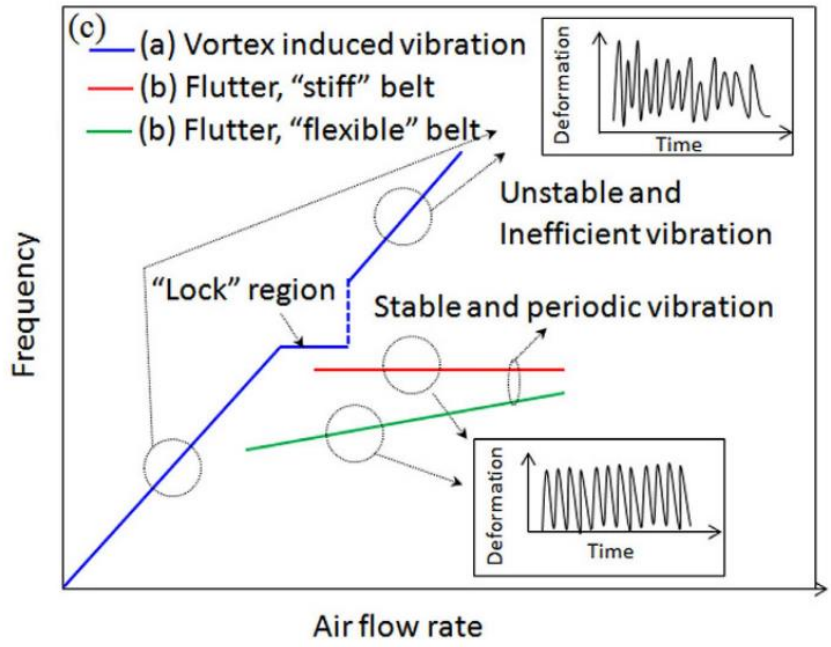


**Fig. 4.16** Comparison of lock-in phenomenon according to fluid structure coupling type

# CHAPTER 5.
# ENHANCEMENT OF DETECTION PERFORMANCE USING MULTI-CHANNEL APPROACH

As a result of the reduced model test, it was found that many false positive signals can occur. False positives are signals that appear in the vertical direction in the time-frequency spectrum. Examples of vertical signals that can be detected as false positives are summarized in Table 5.1 and Fig. 5.1. Candidates for signals that can appear in a vertical form in the waterfall diagram are lock-in, auxiliary machinery local vibration, local structure resonance, and low frequency forced vibration. The characteristics of each are shown in Table 5.1. Among them, auxiliary machinery local vibration and local structure resonance are localized, so they are easily distinguished from the lock-in observed in the entire stern part, and low frequency forced vibration is easily distinguishable because it is not perfectly vertical.

The reason for developing a lock-in detection solution is to automatically detect all lock-ins that occur on a ship using vision artificial intelligence technology. A false negative is a dangerous situation in that it is necessary to filter out problems at the trial run stage, and it is necessary to minimize false negatives by

appropriately adjusting the Pc value, which indicates the probability of the existence of a bounding box in the grid, if possible. In this case, the number of false positives may increase, which may not be appropriate from the point of view of having to judge the problem conservatively.

A method for robustly detecting the signals measured in the stern part without adjusting the Pc value is needed. Previously, vertical vibration components due to local structural resonance or operation of auxiliary machinery appeared only in some sensors in the stern part, whereas in the case of lock-in, it is characterized in that it is measured in the entire stern part. Using this, this study reviewed the multi-channel sensor fusion method. Multi-channel sensor fusion methods include early fusion and late fusion methods as shown in Fig. 5.2. However, since the data theoretically generated for training in this study is one-channel data, it would be difficult to utilize multi-channel input, so the Late Fusion method was applied here. In this case, only the Bounding Box in which the intersection over union(IoU) of each channel is 0.8 or more is left, and an algorithm that determines if it is detected in 90% or more of the total combinations is applied as VIV. Fig. 5.3 shows the concept of the multi-channel voting system applied in this study, and Fig. 5.4 shows the detection result with the reduced model test 3-axis data as input. The false positive disappears, and the lock-in phenomenon is properly detected.

**Table 5.1** Examples of vertical signals that can be detected as false positives

| Vertical signal | Cause | Frequency range | Detection range | Signal characteristics |
|---|---|---|---|---|
| Lock-in | Resonance between structural natural frequency and vortex shedding frequency | Mid, High frequency | global | Occurs in a wider rpm range compared to general structural resonance, prediction is difficult, and hysteresis characteristics |
| Machinery vibration | Auxiliary machinery local vibration(Generator, motor, turbine, pump, etc.) | 60Hz, 30Hz, 15Hz... | local | Narrow band frequency, predictable<br>Occurs in all rpm range |
| Structural resonance | Local structure resonance by low frequency propeller random excitation | Low frequency | local | Broad band frequency, difficult to predict<br>Can occur at multiple operating rpm |
| Low freq. excitation | Forced vibration by propeller and shaft low frequency excitation | Low frequency | global | Frequency change with rpm, predictable,<br>Easily distinguishable because it is not perfectly vertical |

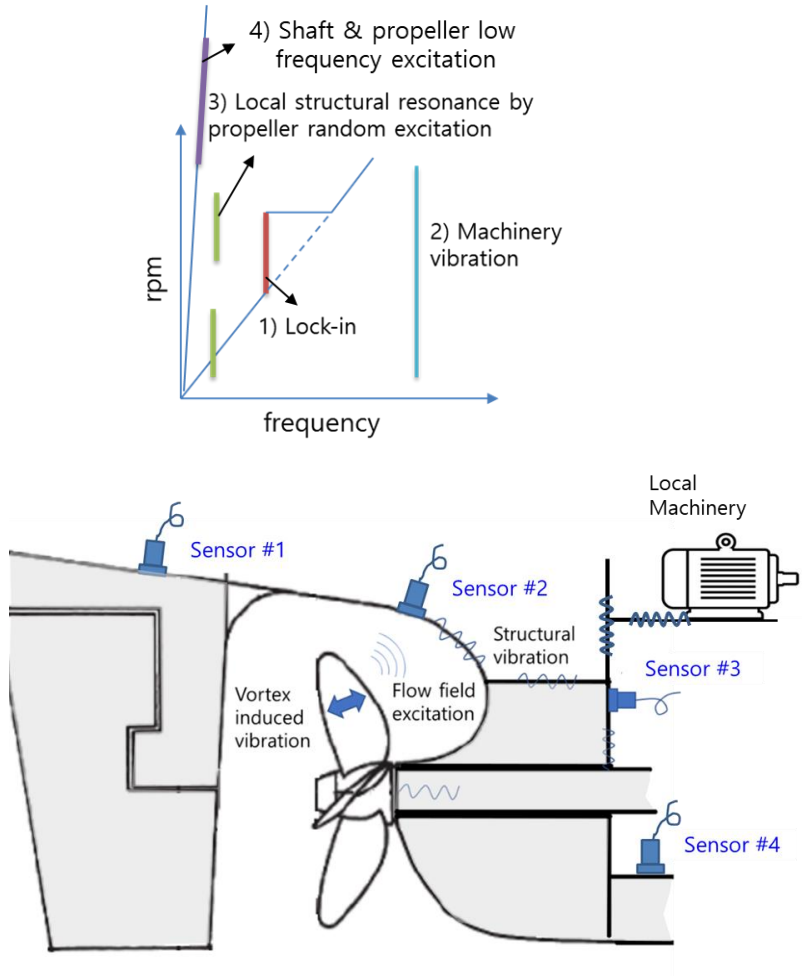


**Fig. 5.1** Examples of vertical signals that can be detected as false positives

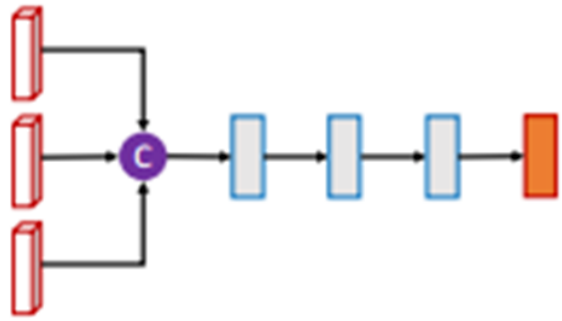


(a) Early Fusion Method

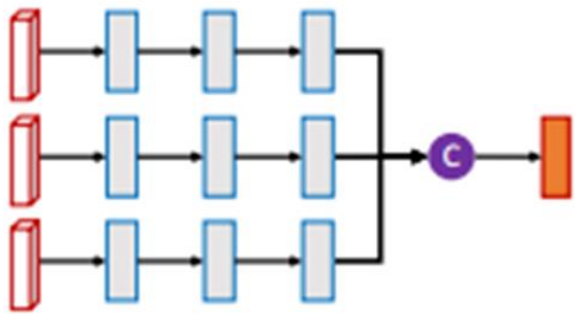


(b) Late Fusion

**Fig. 5.2** Two kinds of muti-channel approach

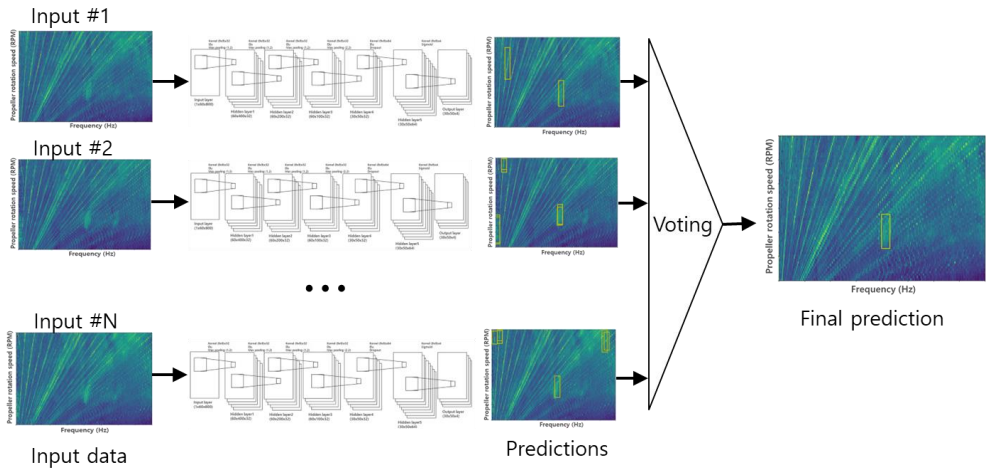


**Fig. 5.3** Concept of multi-channel based lock-in detection system

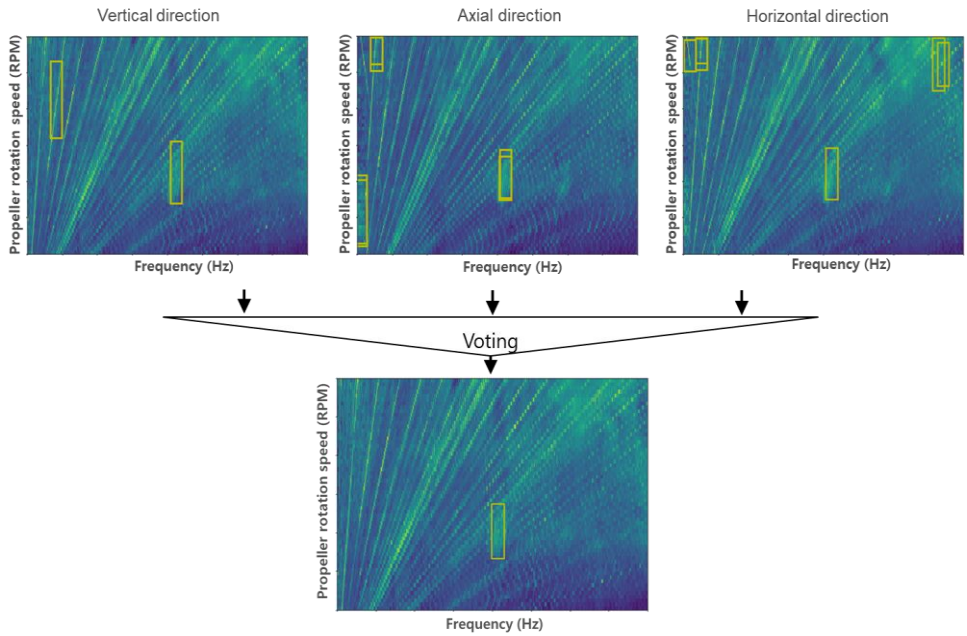


**Fig. 5.4** Multi-channel based lock-in detection system for scaled model data

# CHAPTER 6.
# VORTEX-INDUCED VIBRATION IDENTIFICATION IN THE PROPELLER OF A CRUDE OIL CARRIER

The vibration data from a crude oil carrier in which VIV occurred during the sea trial phase were applied to the VIV detector. Fig. 6.1 shows a typical Very Large Crude Oil Carrier. In the case of the crude oil carrier in the picture, it is sized to carry about 300k dead weight ton of crude oil. Fig. 6.2 shows an example of vibration measured at the stern. As it is difficult to predict the location in a hull at which a propeller vibration component can be observed, measurements were taken at 6 points on the hull structure near the propeller.

Fig. 6.3 shows the vibration values (waterfall charts) measured at 6 points on the stern of the ship. The rotational speeds of the propeller, secured through the sea trial test, range from 50 to 75 RPM at intervals of between 2 or 3 RPM not 1 RPM. In order to make the measured waterfall chart to input data format, linear interpolation was applied in the range of 50 to 75 RPM. Also, in order to use the detector with the input data in the range of 21 to 80 RPM, the speed values lower than 50 RPM and higher than 75 RPM were padded with the smallest value among the data in the range of 50 to 75 RPM.

Fig. 6.4 through Fig. 6.6 show the result of applying the VIV detection algorithm with reference Pc = 0.9. Though the results vary by measurement location, it is evident that lock-in frequencies and RPMs are detected. In particular, the Ch. 2 data measured at the stern tube are detected despite the difficulty with visual observation of the lock-in phenomenon. This data confirms the performance of the detector. Furthermore, some bounding boxes are detected in some sections even though they do not represent lock-in phenomena. These boxes can be distinguished from the ones associated with lock-in phenomena because the former lack consistency by channel. Thus, if a VIV detector is developed in a structure where waterfall charts of different channels are input at the same time, the performance is expected to improve as mentioned in section 4.2.

Figure 6.7 shows the enhancement of detection performance results using multichannel approach proposed in the previous chapter to remove the false positive signal caused by local vibration.


**Fig. 6.1** Example of very large crude oil carrier

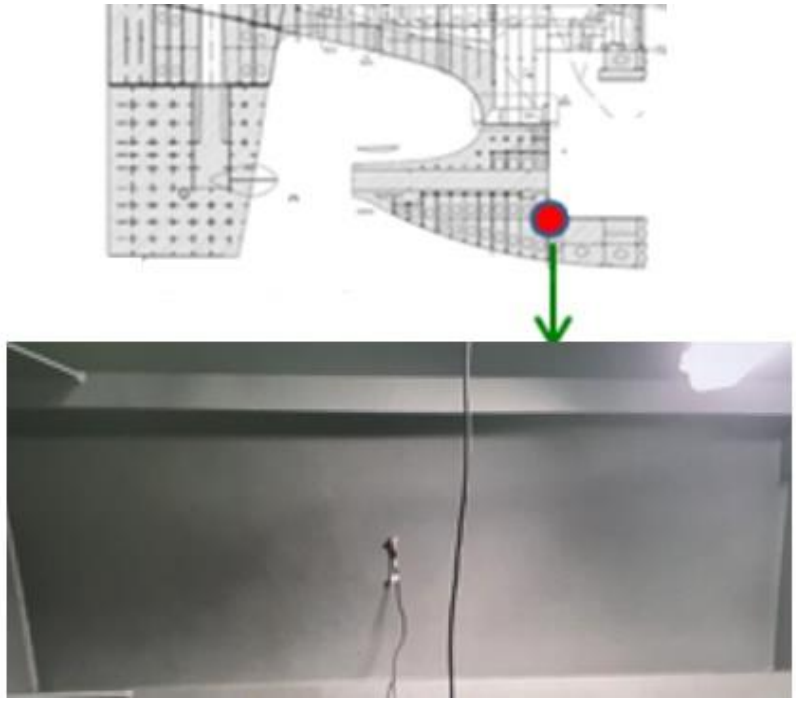

**Fig. 6.2** Example vibration measurement at the stern wall

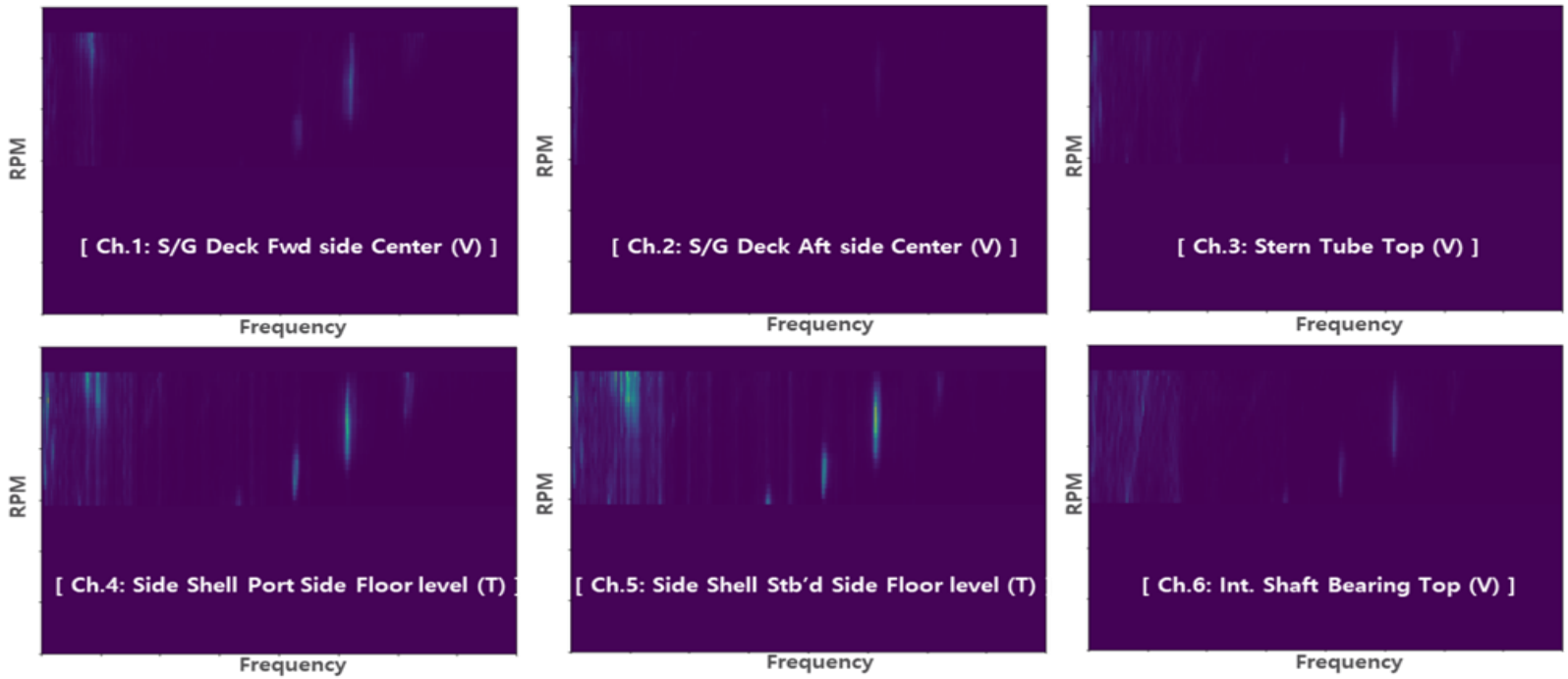


**Fig. 6.3** Post-processing vibration measurement results

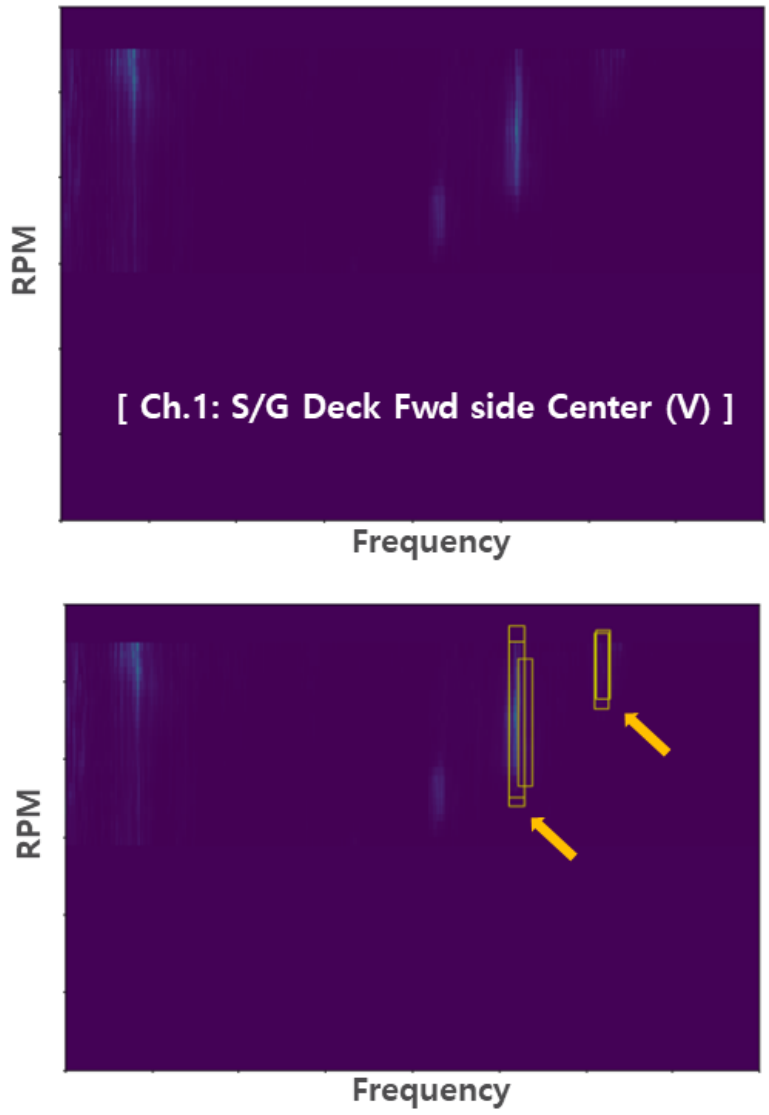


**Fig. 6.4** VIV detection algorithm results (Ch. 1)

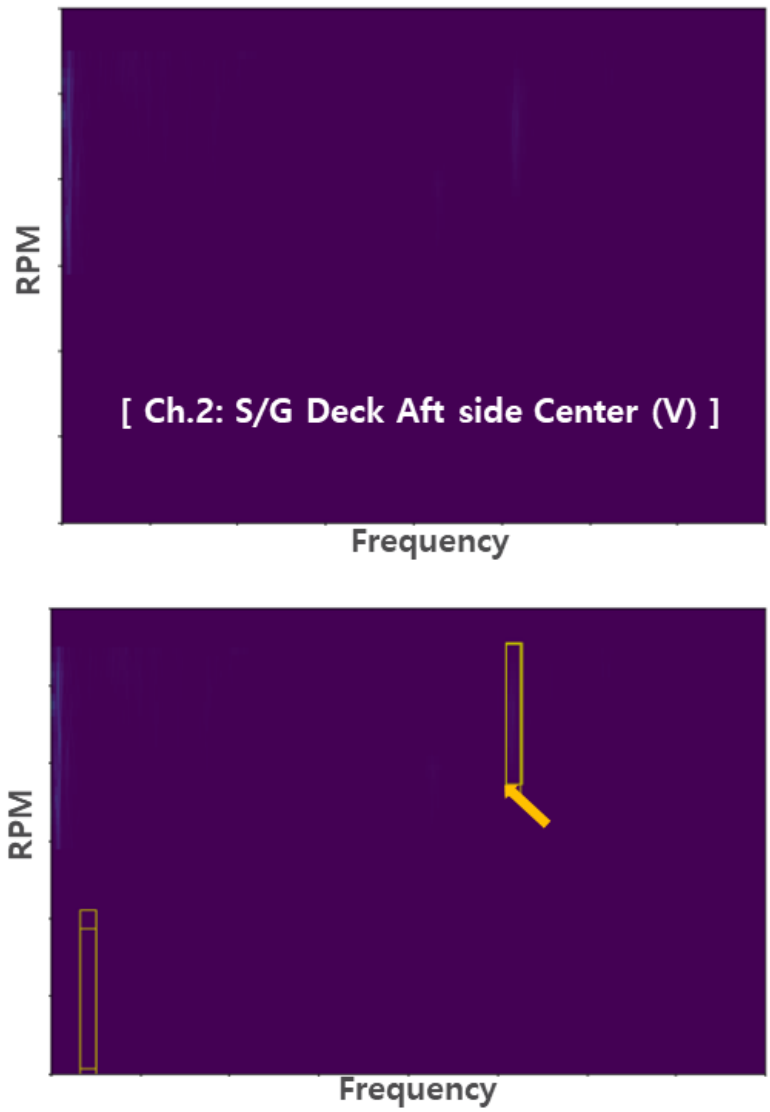


**Fig. 6.5** VIV detection algorithm results (Ch. 2)

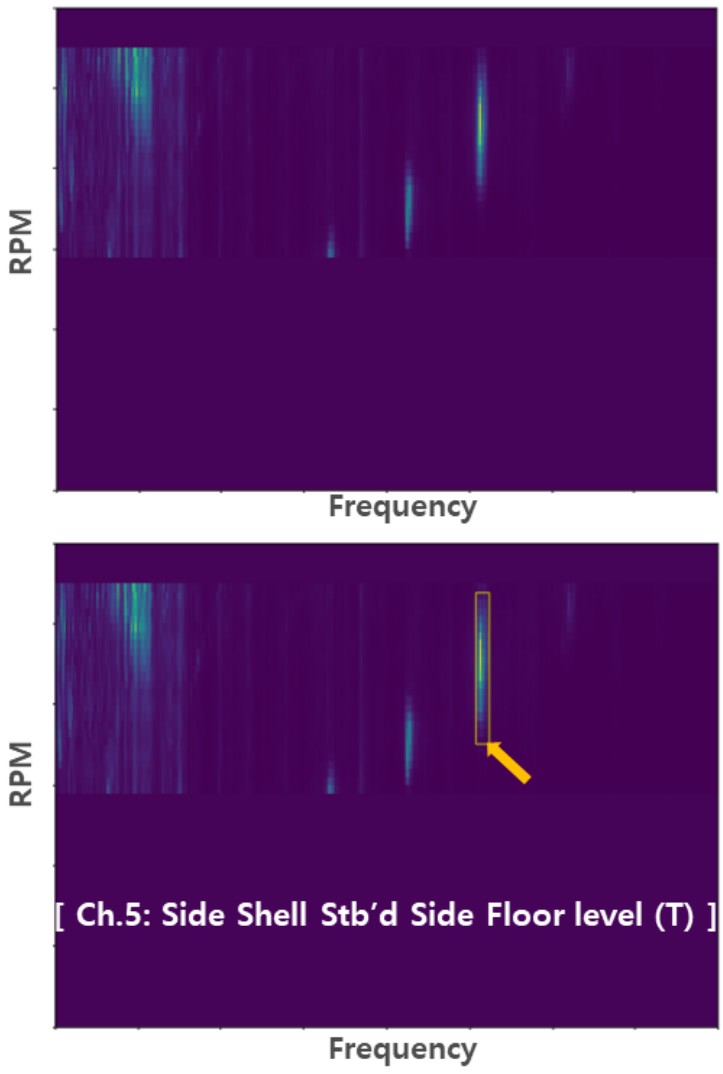


**Fig. 6.6** VIV detection algorithm results (Ch. 5)

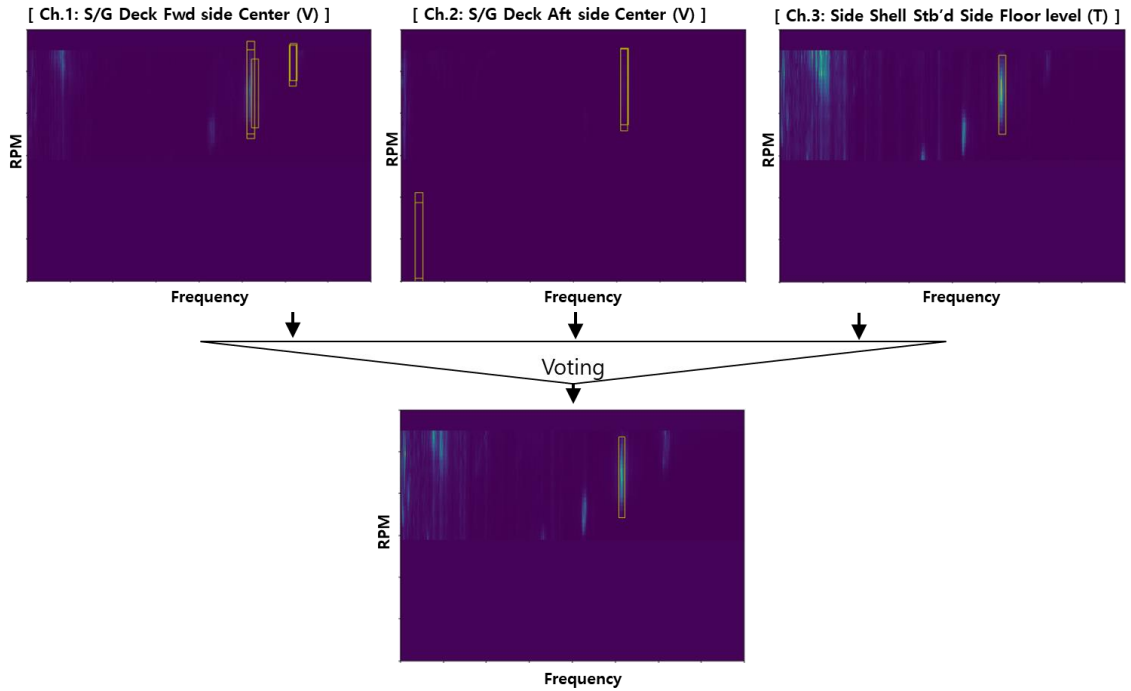


**Fig. 6.7** Enhancement of detection performance using multichannel approach

# CHAPTER 6.
# CONCLUSION

To inspect the VIV phenomenon of ship propellers, it is necessary to review the waterfall chart carefully. The waterfall chart is obtained by classical signal processing on the measured vibration signal. This study's deep learning-based VIV detection algorithm was developed to play the expert's role of reading the waterfall chart to detect the lock-in phenomenon. Noting that the waterfall chart is regarded as a kind of image, we applied the deep learning technology that is effective for image recognition for the present underwater structure diagnosis. This research showed the feasibility of using deep-learning-based detection to detect the VIV phenomenon. In addition, it was shown that VIV-related data, which are difficult to measure directly from rotating propellers, can be acquired indirectly using the vibrations of the in-board stationary structure.

We developed a deep learning algorithm to detect the VIV, a potential cause of the vibration fatigue or singing of the propellers of large merchant ships. Specifically, a CNN (convolutional neural network) was used to automate the VIV detection. A method based on modal superposition is proposed to generate the large amount of data required for training the

network needed in a deep learning algorithm. We used 100,000 data sets and 1,000 data sets for the training and validation of the network, respectively. A subsequent test using 1,000 data sets shows that the diagnostic success rate of the proposed algorithm reaches 82%. The developed algorithm was successfully tested using vibration data acquired in a small-scale system built in a laboratory and applied to a commercial ship during her sea trial operation with satisfactory accuracy. Some findings from the present study and the limitations of the proposed VIV detection algorithm using the proposed method in the actual operational environment of commercial ships may be summarized as follows.

It is essential to identify VIV within the sea trial period as much as possible because it is difficult and costly to resolve the VIV-related issue when it is discovered after the trial operation. Nevertheless, VIV monitoring is necessary even after the sea trial. Depending on the loading conditions of the ship, the draft of the ship changes, and the occurrence of vortex shedding also changes. Because sea trials are conducted in ballast conditions, and full load conditions are included in actual sailing conditions, vortex shedding may vary. Therefore, the monitoring system developed in this study is expected to be usefully used for monitoring after the vessel's delivery.

The proposed VIV detection algorithm is not perfect or fully

developed because it was trained using only artificial data. In addition, its inference accuracy obtained with the test data was 82%, but it may be lower when applied to real data acquired from actual ships. Therefore, the VIV detection algorithm of this research needs to be further tuned or refined and improved in the future. However, it appears that it can still be used for alarming purposes. It was also noted that the false-negative and false-positive ratios depend on the reference Pc value; the false-positive rate increases as the reference Pc value becomes lower, while the false-negative rate increases as the reference Pc value is higher. Lowering the false-negative rate remains an issue to be further overcome for the practical application of the developed algorithm. For example, further studies are needed to determine the Pc threshold to lower the false-negative rate even if the false-positive rate is slightly higher and propose a more elaborate objective function for the training of the VIV detection algorithm. To further increase diagnostic accuracy, it is necessary to accumulate real data labeled by experts and use them to train the VIV detection algorithm.

Although several different network models may be used for monitoring abnormalities as considered in this study, we employed a relatively simple CNN network model. Therefore, considerations of different network models and even developments of new network models will be

worth further investigation. However, we used a simple CNN network model because it has been successful in similar problems to those considered here and its characteristics are also quite well-known. In that this study investigates the feasibility of using a deep-learning-based method for VIV detection, which has not yet been explored, the use of a simple network model may be justified. It is also remarked that the proposed efforts to establish a method to synthesize data for network buildup using a relatively simple yet accurate engineering approach can be another step towards the development of a practically-applicable VIV detection method.

The contribution of this paper may be summarized as follows.

1. A real-time VIV monitoring method using indirect vibration signals that are relatively easy to measure experimentally is proposed.
2. Although the employed network model is relatively simple, we proposed a systematic VIV detection method based on a deep-learning-based data approach.
3. The validity of the proposed model was experimentally confirmed. Thus, the present study opens a new possibility of using big-data approaches for VIV detection in real ships during their sea tests or in their operations.

# REFERENCES

[1] Hyundai Heavy Industries, Hyundai Heavy Industries produces 5,000th propeller. http://www.hyundaiengine.com/about/about12.asp?table=Press&doing=view&idx=11515, 2017 (accessed 13 May 2020).

[2] J. Carlton, Marine propellers and propulsion, second ed., Butterworth-einemann, Oxford, 2007.

[3] J.S. Carlton, D. Vlasi´c, Ship vibration and noise: Some topical aspects, in: Proceedings of the 1st International Ship Noise and Vibration Conference 2005, London, 2006.

[4] D. Shiels, A. Leonard, A. Roshko, Flow-induced vibration of a circular cylinder at limiting structural parameters, J. Fluids Struct. 15 (2001) 3-21.

[5] H. Blackburn, R. Henderson, Lock-in behavior in simulated vortex-induced vibration, Exp. Therm. Fluid Sci. 12 (1996) 184-189.

[6] W. Zhang, X. Li, Z. Ye, Y. Jiang, Mechanism of frequency lock-in in vortex-induced vibrations at low Reynolds numbers, J. Fluid Mech. 783 (2015) 72-102.

[7] W.K. Blake, Mechanics of flow-induced sound and vibration, second ed., Academic Press, Cambridge, MA, 2017.

[8] R. Arndt, P. Pennings, J. Bosschers, T. van Terwisga, The singing vortex, Interface Focus 5 (2015) 20150025.

[9] Z. Liu, B. Wang, X. Peng, D. Liu, Calculation of tip vortex cavitation flows around three-dimensional hydrofoils and propellers using a nonlinear k -ε turbulence model, J. Hydrodynam. 28 (2016) 227-237.

[10] Y.L. Young, Fluid–structure interaction analysis of flexible composite marine propellers, J. Fluids Struct. 24 (2008) 799-818.

[11] Y. LeCun, Y. Bengio, G. Hinton, Deep learning, Nature 521 (2015) 436-444.

[12] M. Raissi, Z. Wang, M.S. Triantafyllou, G.E. Karniadakis, Deep learning of vortex-induced vibrations, J. Fluid Mech. 861 (2019) 119–137.

[13] Y. Bao, Z. Tang, H. Li, Y. Zhang, Computer vision and deep learning–based data anomaly detection method for structural health monitoring, Struct. Health Monit. 18 (2018) 401-421.

[14] J. Guo, X. Xie, R. Bie, L. Sun, Structural health monitoring by using a sparse coding-based deep learning algorithm with wireless sensor networks, Pers. Ubiquit. Comput. 18 (2014) 1977-1987.

[15] S. Sarkar, K. Reddy, M. Giering, M.R. Gurvich, Deep learning for structural health monitoring: a damage characterization application, in: Proceedings of the annual conference of the prognostics and health management society 2016, Denver, 2016.

[16] M. Sohaib, C.-H. Kim, J.-M. Kim, A hybrid feature model and deep-learning-based bearing fault diagnosis, Sensors 17 (2017) 2876.

[17] J. Feng, L. Yaguo, G. Liang, L. Jing, X. Saibo, A neural network

constructed by deep learning technique and its application to intelligent fault diagnosis of machines, Neurocomputing 272 (2018) 619-628.

[18] W. Zhang, G. Peng, C. Li, Y. Chen, Z. Zhang, A new deep learning model for fault diagnosis with good anti-noise and domain adaptation ability on raw vibration signals, Sensors 17 (2017) 425.

[19] J. Liu, Y. Hu, Y. Wang, B. Wu, J. Fan, Z. Hu, An integrated multi-sensor fusion-based deep feature learning approach for rotating machinery diagnosis, Meas. Sci. Technol. 29 (2018)

[20] J. Fu, J. Chu, P. Guo and Z. Chen, Condition monitoring of wind turbine gearbox bearing based on deep learning model, IEEE Access 7 (2019) 57078-57087.

[21] O. Janssens, V. Slavkovikj, B. Vervisch, K. Stockman, M. Loccufier, S. Verstockt, R. Van de Walle, S. Van Hoecke, Convolutional neural network based fault detection for rotating machinery, J. Sound Vib. 377 (2016) 331-345.

[22] R. Liu, G. Meng, B. Yang, C. Sun, X. Chen, Dislocated time series convolutional neural architecture: an intelligent fault diagnosis approach for electric machine, IEEE Trans. Industr. Inf. 13 (2017) 1310-1320.

[23] P. Wang, Ananya, R. Yan, R.X. Gao, Virtualization and deep recognition for system fault classification, J. Manuf. Syst. 44 (2017) 310-316.

[24] W. Sun, B. Yao, N. Zeng, B. Chen, Y. He, X. Cao, W. He, An intelligent gear fault diagnosis methodology using a complex wavelet enhanced convolutional neural network, Materials 10 (2017) 790.

[25] Z. Chen, C. Li, R.-V. Sanchez, Gearbox fault identification and classification with convolutional neural networks, Shock Vib. 2015 (2015) 1-10.

[26] R. Zhao, R. Yan, Z. Chen, K. Mao, P. Wang, R.X. Gao, Deep learning and its applications to machine health monitoring, Mech. Syst.

Signal Process. 115 (2019) 213-237.

[27] TensorFlow, TensorFlow Core v2.3.0. https://www.tensorflow.org/api_docs, 2020 (accessed 13 May 2020).

[28] A. Zobiri, P. Ausoni, F. Avellan, M. Farhat, Vortex shedding from blunt and oblique trailing edge hydrofoils, in: Proceedings of the 3rd IAHR International Meeting of the Workgroup on Cavitation and Dynamic Problems in Hydraulic Machinery and Systems, Brno, Czech Republic, 2009.

[29] X. Glorot and Y. Bengio, “Understanding the difficulty of training deep feedforward neural networks,” Proceedings of Machine Learning Research, vol. 9, pp. 249–256, 2010.

[30] L. Guo, Y. Lei, S. Xing, T. Yan, and N. Li, “Deep Convolutional Transfer Learning Network: A New Method for Intelligent Fault Diagnosis of Machines with Unlabeled Data,” IEEE Transactions on Industrial Electronics, vol. 66, no. 9, pp. 7316–7325, Sep. 2019.

[31] L. S. Maraaba, A. S. Milhem, I. A. Nemer, H. Al-Duwaish, and M. A. Abido, “Convolutional Neural Network-Based Inter-Turn Fault Diagnosis in LSPMSMs,” IEEE Access, vol. 8, pp. 81960–81970, 2020.

[32] Q. Liu and C. Huang, “A Fault Diagnosis Method Based on Transfer Convolutional Neural Networks,” IEEE Access, vol. 7, pp. 171423–171430, 2019.

[33] S. Soetens, A. Sarris, and K. Vansteenhuyse, “A Discriminative Feature Learning Approach for Deep Face Recognition,” in European conference on computer vision, 2016, pp. 499–515.

[34] J. Gu, Z. Wang, J. Kuen, L. Ma, A. Shahroudy, B. Shuai, T. Liu, X. Wang, G. Wang, J. Cai, and T. Chen, “Recent advances in convolutional neural networks,” Pattern Recognition, vol. 77, pp. 354–377, May 2018.

[36] Z. Li, M. Dong, S. Wen, X. Hu, P. Zhou, and Z. Zeng, “CLU-CNNs: Object detection for medical images,” Neurocomputing, vol. 350, pp.

53–59, Jul. 2019.

[37] K. He, X. Zhang, S. Ren, and J. Sun, “Deep residual learning for image recognition,” in Proceedings of the IEEE Computer Society Conference on Computer Vision and Pattern Recognition, 2016, vol. 2016-Decem, pp. 770–778.

[38] K. Simonyan and A. Zisserman, “Very deep convolutional networks for large-scale image recognition,” in 3rd International Conference on Learning Representations, ICLR 2015 - Conference Track Proceedings, 2015.

[39] R. K. Srivastava, K. Greff, and J. Schmidhuber, “Training Very Deep Networks,” in Advances in Neural Information Processing Systems, 2015, pp. 2377–2385.

[40] G. Huang, Z. Liu, L. Van Der Maaten, and K. Q. Weinberger, “Densely connected convolutional networks,” in Proceedings - 30th IEEE Conference 148 on Computer Vision and Pattern Recognition, CVPR 2017, 2017, vol. 2017- January, pp. 2261–2269.

[41] K. He, X. Zhang, S. Ren, and J. Sun, “Deep residual learning for image recognition,” in Proceedings of the IEEE Computer Society Conference on Computer Vision and Pattern Recognition, 2016, vol. 2016-Decem, pp. 770–778.

[42] N. Jin, J. Wu, X. Ma, K. Yan, and Y. Mo, “Multi-task learning model based on multi-scale CNN and LSTM for sentiment classification,” IEEE Access, vol. 8, pp. 77060–77072, 2020.

[43] D. H. Lim, and K. S. Kim, “Development of deep learning-based detection technology for vortex-induced vibration of a ship’s propeller, Journal of Sound and Vibration, Volume 520, 2022.

[44] Y. H. Eom, J. W. Yoo, S. B Hong, M. S. Kim, "Refrigerant charge fault detection method of air source heat pump system using convolutional neural network for energy saving" , Energy, 2019.

[45] M.Y. Kim, J. H. Jung, J. U. Ko, H. B. Kong, J. W. Lee, B. D. Youn, "Direct Connection Based Convolutional Neural Network (DC-CNN) for Fault Diagnosis of Rotor Systems" , IEEE Access, 2020.

ABSTRACT (KOREAN)

# 딥러닝 기반 와류기인 선박 프로펠러 진동 탐지 기술

임 도 형

서울대학교 대학원

기계항공공학부

국제해사기구(IMO)의 탄소 배출량 저감 규제 등의 규제에 따라 조선 해운업계는 선박의 초대형화와 에너지 저감장치(ESD) 등 친환경 장치 적용으로 대응하고 있다. 이에 따라 선박의 프로펠러, 러더, ESD 등 수중 구조물의 설계 변화가 요구되고 있다. 새로운 설계 요구조건에 맞춰 주요 제원이 결정되며 전산유체해석 및 수조시험을 통한 성능설계, 진동해석 및 구조강도해석을 통한 구조설계가 진행된다. 수중구조물 제작 이후에는 품질검사를 거쳐 시운전 중에 성능과 진동평가를 마치면 선박이 인도된다. 친환경 장치가 설치된 대형 상선의 선미 구조물은 형상이 복잡하여 유동 및 진동특성의 설계 민감도가 크고 생산 공차에 따른 피로수명의 산포가 크기 때문에 초기 설계단계에서 모든 품질문제를 걸러 내기 어려운 문제가 있다. 특히 유동장에 있는 수중구조물의 경우 특정 유속에서 와류 이탈이 발생하게 되며 와류 이탈 주파수가 구조물의 고유진동수가 일치하는 경우 공진에 인한 와류기인진동(Vortex Induced Vibration; VIV) 문제가 종종 발생되어 수중구조물 피로손상의 원인이 되고 있다. VIV 문제가 있는 상태로 선박이

인도될 경우 설계수명을 만족하지 못하고 단기간에 파손이 되는 경우가 많아 조선소에 큰 피해를 주기 때문에 선박 인도 직전인 선박 시운전 단계에서 진동이나 응력 계측을 통해 VIV 발생 여부의 확인이 필요하다. 구조물에 작용하는 하중을 계측하는 전통적인 방법은 구조물에 스트레인게이지를 설치하고 수중 텔레미터리를 설치하여 구조물의 스트레인을 직접 계측하는 방법이지만 계측을 위해 많은 비용이 소요되고 계측 실패의 가능성이 매우 높다는 문제가 있다. 본 논문에서는 대형 상선 프로펠러의 대표적인 손상 원인인 Vortex Induced Vibration을 시운전 단계에서 선체 진동 계측을 통해 간접적으로 검출할 수 있는 방법을 제안하였다. 특정 VIV가 문제가 되는 경우는 유속에서 와류 이탈 주파수가 구조물의 고유진동수가 일치하는 경우 공진에 의해 와류이탈 강도가 증가하고 유속이 증가하더라도 와류이탈 주파수가 유지되는 Lock-in 현상이 발생하는 경우로 간접 계측을 통해 이를 명시적으로 확인할 수 있다. 이를 위해서는 진동 전문가의 반복적인 진동 계측 및 평가 프로세스가 필요한데 본 연구에서는 전문가를 대신한 딥러닝 알고리즘을 이용한 VIV 탐지 시스템을 제안하였다. 진동 분석과 VIV 검출 자동화를 위해 이미지 기반의 Object detection을 위해 널리 이용되고 있는 CNN(Convolution Neural Network) 알고리즘을 이용하였다. 본 연구에서는 Object detection을 수행하되 Classification은 수행하지 않아도 되는 특징이 있어 이에 특화된 CNN 모델 개발을 위해 Hyper parameter를 조정하여 Hidden Layer를 증가하는 방법으로 30개의 CNN모델을 검토하였고 최종적으로 과적합이 없이 탐지 성능이 높은 5개의 Hidden layer

가진 모델을 제안하였다. CNN 학습을 위해 필요한 대규모의 데이터 생성을 위해 진동 모드 중첩법 기반의 간이 선박 모델을 제안하였고 프로펠러 기진력을 모사하였다. 간이 모델을 이용하여 실제 진동계측 결과와 유사한 진동 특성을 보이는 10,000개의 데이터를 생성하여 학습에 이용하였고 1,000개의 데이터를 이용하여 테스트한 결과 82%이상의 탐지 성공률을 보였다. 제안된 탐지시스템의 검증을 위해 축소모델 시험을 수행하였다. 프로펠러에서 Vortex shedding 주파수와 블레이드의 수중 고유진동수가 일치하도록 설계된 1/10 스케일의 선박 추진 시스템 축소 모델을 이용하여 프로펠러에서 Vortex Induced Vibration을 발생시키고 프로펠러 주변 구조물에서 가속도계를 이용하여 Lock-in 현상에 의한 진동을 측정하였다. 이 신호를 이용하여 개발된 시스템으로 VIV의 검출이 가능함을 보였다. 마지막으로 VIV문제가 발생했던 원유운반선의 시운전 중 기관실 내에서 계측된 선체 구조 진동값을 이용하여 개발된 탐지 시스템의 타당성을 검증하고 실제 선박에서의 적용 가능성도 확인하였다. 개발된 시스템은 VIV 검출은 위한 자동화 시스템으로 활용이 가능할 것으로 보이며 향후 실선 데이터가 확보될 경우 유용성이 증가할 것으로 기대된다.

**주요어: 선박 프로펠러 진동, 와류 기인 진동, 진동 기반 모니터링, 딥러닝(DL), 합성곱 신경망(CNN)**
**학번: 2013-30770**